

# Uncertainty-aware Validation Benchmarks for Coupling Free Flow and Porous-Medium Flow

Farid Mohammadi<sup>1</sup>, Elissa Eggenweiler<sup>2</sup>, Bernd Flemisch<sup>1</sup>, Sergey Oladyshkin<sup>1</sup>, Iryna Rybak<sup>2</sup>, Martin Schneider<sup>1</sup>, Kilian Weishaupt<sup>1</sup>

<sup>1</sup>University of Stuttgart, Institute for Modelling Hydraulic and Environmental Systems

<sup>2</sup>University of Stuttgart, Institute of Applied Analysis and Numerical Simulation

## Abstract

A correct choice of interface conditions and useful model parameters for coupled free-flow and porous-medium systems is vital for physically consistent modeling and accurate numerical simulations of applications. We consider the Stokes–Darcy problem with different models for the porous-medium compartment and corresponding coupling strategies: the standard averaged model based on Darcy’s law with classical or generalized interface conditions as well as the pore-network model. We study the coupled flow problems’ behaviors considering a benchmark case where a pore-scale resolved model provides the reference solution and quantify the uncertainties in the models’ parameters and the reference data. To achieve this, we apply a statistical framework that incorporates a probabilistic modeling technique using a fully Bayesian approach. A Bayesian perspective on a validation task yields an optimal bias-variance trade-off against the reference data. It provides an integrative metric for model validation that incorporates parameter and conceptual uncertainty. Additionally, a model reduction technique, namely Bayesian Sparse Polynomial Chaos Expansion, is employed to accelerate the calibration and validation processes for computationally demanding Stokes–Darcy models with different coupling strategies. We perform uncertainty-aware validation, demonstrate each model’s predictive capabilities, and make a model comparison using a Bayesian validation metric.

## 1 Introduction

Coupled free-flow and porous-medium systems play a significant role in many industrial, environmental, and biological settings, e.g., fuel cells, water flows in karst aquifers, blood flows in vessels and living tissues. Flow interaction between the free-flow region and the porous-medium domain is extremely involved and strongly interface-driven. Therefore, a physically consistent description of flow processes in the whole coupled system and especially near the interface is crucial for accurate numerical simulations of applications. A lot of effort has been made during the last decades in mathematical modeling and analysis of such coupled systems, and several coupling strategies have been proposed, e.g. (Angot et al., 2017; Discacciati & Quarteroni, 2009; Goyeau et al., 2003; Jäger & Mikelić, 2009; Lācis & Bagheri, 2017; Ochoa-Tapia & Whitaker, 1995). The most widely studied problem in the literature is the Stokes–Darcy problem. In this case, the Stokes equations describe the flow in the free-flow domain; Darcy’s law describes fluid flow through the porous medium, and the appropriate set of coupling conditions is imposed on the fluid–porous interface.

The coupled macroscale Stokes–Darcy model with the classical set of interface conditions contains a version of the Beavers–Joseph condition which was postulated for one-dimensional flows parallel to the porous layer (Beavers & Joseph, 1967). Later, the simplified Beavers–Joseph–Saffman condition was rigorously derived using the theory of homogenisation and boundary layers (Jäger & Mikelić, 2009; Saffman, 1971).

---

Corresponding author: F. Mohammadi, [farid.mohammadi@iws.uni-stuttgart.de](mailto:farid.mohammadi@iws.uni-stuttgart.de)

Both the Beavers–Joseph condition and its modification by Saffman are not suitable for arbitrary flow directions (Eggenweiler & Rybak, 2020), however, are routinely applied in the literature to multi-dimensional flows (Discacciati & Gerardo-Giorda, 2018; Hanspal et al., 2009). In this paper, we focus on three uncertain parameters in the classical coupled Stokes–Darcy model: the exact interface position, the Beavers–Joseph coefficient and the permeability tensor. The exact location of the fluid–porous interface for macroscale models is not known a priori. In the literature, there are several recommendations to impose the sharp fluid–porous interface directly on the top of solid inclusions in case of circular grains (Lācis et al., 2020; Rybak et al., 2021). For other pore geometries, especially in the case of anisotropic media, the problem of optimal interface location is still open. However, the exact interface location is very important, especially for microfluidic models (Terzis et al., 2019) which are routinely used in experiments. Another uncertain parameter is the Beavers–Joseph coefficient  $\alpha_{BJ}$ , which is supposed to contain the information on the surface roughness (Beavers & Joseph, 1967; Le Bars & Worster, 2006). An investigation to calibrate this parameter was recently carried out in Rybak et al. (2021), however, only for isotropic media. There was also an attempt to determine the Beavers–Joseph coefficient experimentally for flows parallel to the fluid–porous interface, isotropic and orthotropic porous media (Mierzwiczak et al., 2019), where the Beavers–Joseph parameter was found to be  $\alpha_{BJ} < 1$  and dependent on the intrinsic permeability. In Yang et al. (2019), it is demonstrated that  $\alpha_{BJ}$  should not be constant but vary along the interface depending on the flow direction near the porous bed. Finally, the permeability tensor appearing in the Beavers–Joseph condition is not necessarily the permeability of the porous bulk, as in the standard models (Discacciati et al., 2002; Discacciati & Quarteroni, 2009), but could also be permeability of the near-interfacial region (Lācis & Bagheri, 2017; Zampogna & Bottaro, 2016). These three uncertain parameters will be studied in the paper for a specific geometrical configuration. Moreover, the classical macroscale model will be compared against two other coupling concepts: the Stokes–Darcy model with the generalized coupling conditions and the pore-network model in the interfacial zone.

For the generalized coupling conditions derived rigorously in Eggenweiler and Rybak (2021), the interface can be located at the distance  $\mathcal{O}(\ell)$  from the top of the first row of solid inclusions. Based on this choice of the interface position, the effective coefficients are computed numerically. This is the main advantage of the generalized interface conditions. The permeability tensor and all the effective coefficients appearing in the new conditions are computed numerically using the theory of homogenisation and boundary layers (Carraro et al., 2015; Hornung, 1997; Jäger & Mikelić, 2000, 2009) based on the pore geometry. These conditions will be used for the inter-comparison with the classical interface conditions and the pore-network model. There are other alternative coupling concepts in the literature for Stokes–Darcy problems, e.g. (Angot et al., 2017, 2021; Lācis et al., 2020; Ochoa-Tapia & Whitaker, 1995) which are beyond the scope of this manuscript. Pore-network models (Blunt, 2017) consider a simplified yet equivalent representation of the porous geometry by separating the void space into larger pore bodies connected by narrow pore throats. Despite their low computational demand, a rather high degree of pore-scale accuracy can be achieved (Oostrom et al., 2016). They can also be combined with modeling approaches on different scales (Scheibe et al., 2015), such as Darcy-type continuum models (Balhoff, Thompson, & Hjortsø, 2007; Balhoff, Thomas, & Wheeler, 2007; Mehmani & Balhoff, 2014) or free-flow models (Beyhaghi et al., 2016). (Weishaupt et al., 2019) developed a fully implicit and monolithic approach to couple a pore-network model with a (Navier–)Stokes model, which was later improved by considering pore-scale slip (Weishaupt et al., 2020).

According to the discussion above, there are various possibilities to conceptualize the coupling of free flow and porous-medium flow that could be seen as conceptual

uncertainty. The conceptual uncertainty is mainly related to the description of processes in the porous medium, for which different mathematical models are considered. The free-flow conceptualization is based on the standard Stokes equations for all discussed models. Apart from the conceptual uncertainty, each computational model contains parametric uncertainty, such as upscaling parameters, material parameters, or interface location that should also be rigorously addressed. Therefore, a significant research challenge is to accurately assess competing modeling concepts and validate the corresponding computational models against an experiment or a reference solution. Following the guidelines for validation benchmarks in (Oberkampf & Roy, 2010) and as well in (Oberkampf & Trucano, 2008), the most important scientific question to be addressed here is how to compare quantitatively the computational models. Each validation benchmark has to declare one or more methods that should be employed for quantitative comparison. The development of such validation metrics is an active field of research. While being potentially applicable to many research areas, rigorously developed validation metrics have been applied to some of them only, such as computational fluid dynamics (Oberkampf & Barone, 2006), computational solid mechanics (Mahadevan & Rebba, 2005) or heat transfer (Hills, 2006). To the best of our knowledge, no rigorous development and application of uncertainty-aware validation has been carried out for the coupling of free flow and porous-medium flow. To tackle this challenge, we will employ an uncertainty-aware validation metric that relies on the Bayesian analysis of the competing models.

A Bayesian perspective on a validation task yields an optimal bias-variance trade-off against the experimental data (or reference solution). It provides an integrative metric for model validation that incorporates parameter and conceptual uncertainty (Geman et al., 1992; Schöniger et al., 2014, 2015). Following the Bayesian model selection pathway, we will employ the Bayesian model evidence (BME) as a validation score indicating the quality of the analyzed physical models against the available experimental data or finely resolved reference solution. The Bayesian validation framework, relying on the BME values, requires propagating the parametric uncertainty through all competing models, conceptualizing the coupling of free flow and porous-medium flow. The probabilistic nature of the Bayesian technique requires a significant number of model evaluations to reach statistical convergence. In practice, however, the computational complexity of the underlying computational model and the total available computational budget severely restrict the number of evaluations that one can carry out. This challenge renders the brute-force computation of the BME value required for the Bayesian validation framework infeasible. We will replace the original computational model with its easy-to-evaluate surrogate in the Bayesian analysis. A surrogate model’s main goal is to replicate the behavior of the underlying physical models from a limited set of runs without sacrificing the accuracy.

For constructing a surrogate, a computational model should be evaluated using those sets of modeling parameters, out of various possibilities, that cover the parametric space as well as possible. The polynomial chaos expansion (PCE) (Wiener, 1938) or its extension toward arbitrary polynomial chaos expansion (aPCE) (Oladyshkin & Nowak, 2012) is a well known and rigorous approach providing functional representations of stochastic quantities. However, not all expansion terms are relevant for the representation of the underlying physical processes and employing the concept of sparsity can lead to zero values for many coefficients in the expansion (Tipping, 2001). There are many mathematical approaches when dealing with a regression problem such as PCE representation that lead to a sparse solution. These approaches have led to the emergence of numerous sparse solvers in the compressed sensing (Arjouni et al., 2017), as well as in the sparse PCE. In (Lüthen et al., 2021), the authors provide a comprehensive survey of the proposed solvers in the context of PCE. Here, we employ Bayesian sparse aPCE denoted as BsaPCE, which is an extension of aPCE within a Bayesian framework by means of a Bayesian sparse learning method (Tipping

et al., 2003). BsaPCE not only identifies the relevant expansion terms which capture the relevant features of the physical model, but it is also able to provide a probabilistic prediction, i.e. a prediction with the associated uncertainty. This prediction uncertainty can be used as the expected error occurring when replacing the original computational model by a possibly less accurate surrogate.

The rest of this paper is organized as follows. In Section 2, the mathematical and computational models are presented that are going to be evaluated by means of the proposed benchmark scenario. The Bayesian validation framework is introduced in Section 3. The scenario is described in Section 4, while Section 5 is devoted to a discussion of the application of the Bayesian framework. The paper is concluded in Section 6.

## 2 Mathematical and Computational Models

From a pore-scale perspective, we consider a two-dimensional flow domain  $\Omega_{\text{flow}}$  consisting of a free-flow domain  $\Omega_{\text{ff}}$  and the pore space  $\Omega_{\text{pore}}$  of the porous medium,  $\Omega_{\text{flow}} = \Omega_{\text{ff}} \cup \Omega_{\text{pore}}$ . The porous-medium domain  $\Omega_{\text{pm}}$  has a periodic structure composed by the repetition of the REV (scaled unit cell)  $Y^\ell = (0, \ell) \times (0, \ell)$ , where  $\ell = 0.5$  [mm] is the microscopic length scale (Figure 1, left). From a macroscopic point of view, the coupled domain  $\Omega$  comprises the free-flow region  $\Omega_{\text{ff}}$  and the porous-medium domain  $\Omega_{\text{pm}}$ , separated by a sharp fluid-porous interface  $\Gamma$  (Figure 1, right).

We consider isothermal single-phase flow at low Reynolds numbers. The same fluid

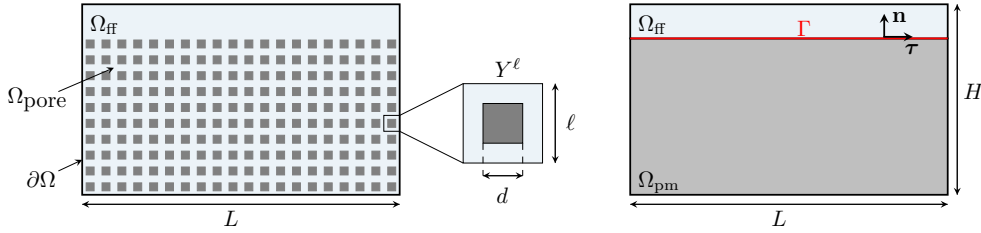


**Figure 1.** Geometrical setting at the pore scale (left) and macroscale (right).

occupies the free-flow domain and fully saturates the porous medium. This fluid is supposed to be incompressible and to have constant viscosity. We consider a non-deformable porous medium leading to constant porosity  $\phi$ .

### 2.1 Pore-scale Resolved Model

At the pore scale, fluid flow in the whole flow domain  $\Omega_{\text{flow}}$  is governed by the Stokes equations

$$\nabla \cdot \mathbf{v} = 0, \quad -\nabla \cdot \mathbf{T}(\mathbf{v}, p) = \mathbf{0} \quad \text{in } \Omega_{\text{flow}}, \quad (1)$$

completed with the no-slip condition on the boundary of solid inclusions

$$\mathbf{v} = \mathbf{0} \quad \text{on } \partial\Omega_{\text{flow}} \setminus \partial\Omega, \quad (2)$$

and the appropriate conditions on the external boundary  $\partial\Omega$ . Here,  $\mathbf{v}$  and  $p$  denote the fluid velocity and pressure,  $\mathbf{T}(\mathbf{v}, p) = \mu \nabla \mathbf{v} - p \mathbf{I}$  the stress tensor,  $\mathbf{I}$  the identity tensor and  $\mu$  the dynamic viscosity.

Resolving pore-scale information is computationally expensive for practical applications. Therefore, macroscale model formulations, which accurately reflect the pore-scale flow processes, will be studied. The pore-scale resolved model (1)–(2) will be used only for the model validation purposes in Section 4. A finite-volume scheme

on staggered grids, also known as MAC scheme (Harlow & Welch, 1965), is used to discretize the pore-scale model (1)–(2).

## 2.2 Subdomain Models

In this study, we consider two different types of coupled models, where the free-flow region  $\Omega_{\text{ff}}$  and the porous domain  $\Omega_{\text{pm}}$  are treated by different model concepts. The first type relies on the classical REV-scale description of the porous-medium domain using Darcy’s law, whereas the second type of model follows a hybrid-dimensional approach, where an effectively lower-dimensional pore-network model is used to treat the porous domain (Weishaupt et al., 2019, 2020).

*Free flow.* As a common feature, both coupled models (REV-scale model, pore-network model) contain the incompressible, stationary Stokes equations for the description of fluid flow in the free-flow domain  $\Omega_{\text{ff}}$ :

$$\nabla \cdot \mathbf{v}_{\text{ff}} = 0, \quad -\nabla \cdot \mathbf{T}(\mathbf{v}_{\text{ff}}, p_{\text{ff}}) = \mathbf{0} \quad \text{in } \Omega_{\text{ff}}, \quad (3)$$

where  $\mathbf{v}_{\text{ff}}$  is the fluid velocity and  $p_{\text{ff}}$  is the fluid pressure. For discretization of equations (3), the same MAC scheme as for model (1)–(2) is employed.

*REV-scale porous-medium model.* Fluid flow through the porous medium is described by the Darcy flow equations

$$\nabla \cdot \mathbf{v}_{\text{pm}} = 0, \quad \mathbf{v}_{\text{pm}} = -\frac{\mathbf{K}}{\mu} \nabla p_{\text{pm}} \quad \text{in } \Omega_{\text{pm}}, \quad (4)$$

where  $\mathbf{v}_{\text{pm}}$  is the Darcy fluid velocity,  $p_{\text{pm}}$  is the fluid pressure and  $\mathbf{K}$  is the intrinsic permeability tensor, which is symmetric, positive definite and bounded. Equations (4) are discretized with a vertex-centered finite-volume scheme, also known as box method (Hackbusch, 1989). This scheme has the advantage that degrees of freedom are naturally located at the interface and therefore directly allow the calculation of interfacial quantities occurring in the coupling conditions (10)–(12) below.

*Pore-network porous-medium model.* For the pore-network model, we require the continuity of mass at each pore body (the intersection of two or more pore throats):

$$\sum_j Q_{ij} = 0, \quad Q_{ij} = g_{ij}(p_i - p_j). \quad (5)$$

Here,  $Q_{ij}$  is the discrete volume flow rate in a throat connecting the pore bodies  $i$  and  $j$ , and the pressures defined at the centers of the pore bodies  $i$  and  $j$  are given by  $p_i$  and  $p_j$  (Figure 2). The total conductance  $g_{ij}$  is determined by the pore throat

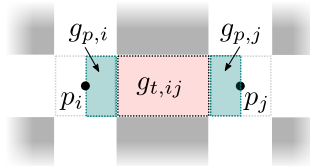


**Figure 2.** Schematic contribution to total conduction for the PNM. Throat  $ij$  connects the pore bodies  $i$  and  $j$  at the centers of which the pressures  $p_i$  and  $p_j$  are defined.  $g_{t,ij}$  is the throat conductance valid for the region marked in light red.  $g_{p,i}$  and  $g_{p,j}$  are the conductances defined for the pore body halves marked in teal.

geometry and the fluid properties. Considering the pressure losses both within the pore bodies and throats, we use

$$g_{ij} = (g_{t,ij}^{-1} + g_{p,i}^{-1} + g_{p,j}^{-1})^{-1}, \quad (6)$$

where  $g_{t,ij}$  is the conductance of throat  $ij$  while  $g_{p,i}$  and  $g_{p,j}$  are the conductances of the adjacent pore-body halves (Figure 2). Simple analytical expressions for  $g_{ij}$  are available in the literature (Patzek & Silin, 2001) for certain geometries. Here, we determine  $g_{ij}$  via numerical upscaling (Mehmani & Tchelepi, 2017) as described in detail in the appendix of (Weishaupt et al., 2019). In the following, we will only refer to  $g_{p,i}$ , as for the given geometry  $g_{p,i} = g_{p,j}$  for interior throats. At interface throats, one of the half-pore-body conductance is zero.

### 2.3 Coupling Concepts

A variety of coupling concepts for the Stokes–Darcy system (3)–(4) is available in the literature. In this paper, we consider the most widely used set of interface conditions based on the Beavers–Joseph condition and recently developed generalized conditions (Eggenweiler & Rybak, 2021). If the pore-network model (5) is used in the porous medium, separate coupling conditions have to be considered.

*Classical coupling conditions (REV-scale model).* The most commonly used interface conditions are the *conservation of mass*

$$\mathbf{v}_{\text{ff}} \cdot \mathbf{n} = \mathbf{v}_{\text{pm}} \cdot \mathbf{n} \quad \text{on } \Gamma, \quad (7)$$

the *balance of normal forces*

$$-\mathbf{n} \cdot \mathbf{T}(\mathbf{v}_{\text{ff}}, p_{\text{ff}}) \mathbf{n} = p_{\text{pm}} \quad \text{on } \Gamma, \quad (8)$$

and the *Beavers–Joseph condition* (Beavers & Joseph, 1967) for the tangential component of velocity

$$(\mathbf{v}_{\text{ff}} - \mathbf{v}_{\text{pm}}) \cdot \boldsymbol{\tau} - \frac{\sqrt{\mathbf{K}}}{\alpha_{\text{BJ}}} \boldsymbol{\tau} \cdot \nabla \mathbf{v}_{\text{ff}} \mathbf{n} = 0 \quad \text{on } \Gamma. \quad (9)$$

Here,  $\alpha_{\text{BJ}} > 0$  is the Beavers–Joseph parameter,  $\mathbf{n}$  is the normal unit vector on  $\Gamma$  pointing outward from the porous medium,  $\boldsymbol{\tau}$  is a tangential unit vector on  $\Gamma$  and  $\sqrt{\mathbf{K}} = \sqrt{\boldsymbol{\tau} \cdot \mathbf{K} \boldsymbol{\tau}}$ .

Although the coupling conditions (7)–(9) are unsuitable for arbitrary flows to the porous bed (Eggenweiler & Rybak, 2020), they are widely used in the literature for different flow scenarios.

*Generalized coupling conditions for arbitrary flows (REV-scale model).* Generalized interface conditions valid for arbitrary flow directions to the fluid–porous interface are rigorously derived in (Eggenweiler & Rybak, 2021) using the theory of homogenization and boundary layers. They amount to

$$\mathbf{v}_{\text{ff}} \cdot \mathbf{n} = \mathbf{v}_{\text{pm}} \cdot \mathbf{n} \quad \text{on } \Gamma, \quad (10)$$

$$p_{\text{pm}} = -\mathbf{n} \cdot \mathbf{T}(\mathbf{v}_{\text{ff}}, p_{\text{ff}}) \mathbf{n} + N_s^{\text{bl}} \boldsymbol{\tau} \cdot \nabla \mathbf{v}_{\text{ff}} \mathbf{n} \quad \text{on } \Gamma, \quad (11)$$

$$\mathbf{v}_{\text{ff}} \cdot \boldsymbol{\tau} = -\ell N_1^{\text{bl}} \boldsymbol{\tau} \cdot \nabla \mathbf{v}_{\text{ff}} \mathbf{n} + \ell^2 \sum_{j=1}^2 \mathbf{M}^{j,\text{bl}} \frac{\partial p_{\text{pm}}}{\partial x_j} \cdot \boldsymbol{\tau} \quad \text{on } \Gamma. \quad (12)$$

Here,  $\mathbf{M}^{j,\text{bl}}$ ,  $N_1^{\text{bl}}$  and  $N_s^{\text{bl}}$  are the boundary layer constants introduced in (Eggenweiler & Rybak, 2021), which are computed numerically based on the pore geometry.

*Coupling conditions for the pore-network model.* Each intersection of a pore body  $i$  with the free-flow domain boundary yields a pore-local discrete interface  $\Gamma_i$  on which we formulate coupling conditions (Figure 3). We assume no-flow/no-slip condition for the free flow at the location of solid grains (no intersecting pore throat). This results in

$$\mathbf{v}_{\text{ff}} \cdot \mathbf{n} = \mathbf{v}_{\text{pm}} \cdot \mathbf{n} \quad \text{on } \Gamma_i, \quad (13)$$

$$p_{\text{pm}} = p_{\text{ff}} \quad \text{on } \Gamma_i, \quad (14)$$

$$\mathbf{v}_{\text{ff}} \cdot \boldsymbol{\tau} = \begin{cases} v_{\text{slip}} & \text{on } \Gamma_i, \\ 0 & \text{else,} \end{cases} \quad (15)$$

with

$$v_{\text{slip}} = \frac{1}{\beta_{\text{pore}}} [-(\nabla \mathbf{v} + \nabla \mathbf{v}^T) \mathbf{n}] \cdot \boldsymbol{\tau}_{\text{ff}} + [\mathbf{v} \cdot \boldsymbol{\tau}]_{\text{pm}}. \quad (16)$$

We approximate the tangential component of the pore-body interface velocity as

$$[\mathbf{v} \cdot \boldsymbol{\tau}]_{\text{pm}} = \frac{Q_{ij}}{|\Gamma_i|} [\mathbf{n}_{ij} \cdot \boldsymbol{\tau}]_{\text{pm}}, \quad (17)$$

where  $\mathbf{n}_{ij}$  is a unit normal vector parallel to the throat's central axis and pointing towards the interface  $\Gamma_i$ , the volume flow through pore throat  $ij$  is given by  $Q_{ij}$  and  $|\Gamma_i|$  is the area of the discrete coupling interface.

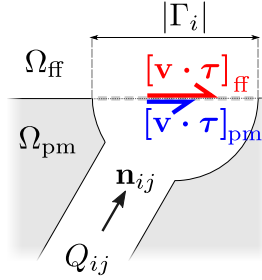


**Figure 3.** Schematic representation of local interface for the free-flow/pore-network model.

Equations (15) and (16) can be seen as the pore-scale analog to Equation (9) with a pore-local slip coefficient  $\beta_{\text{pore}}$ , which is determined numerically in a preprocessing step. We refer to (Weishaupt et al., 2020) for more details.

The three sets of coupling conditions listed above are discretized corresponding to the adjacent subdomain models' discretizations, and the resulting coupled discrete models are treated by a monolithic strategy, assembling all contributions in a single system of equations for each model.

### 3 Bayesian Validation Framework

Several conceptual representations for the coupling of free-flow and porous medium flow have been presented in Section 2. In the current Section, we offer a Bayesian validation framework to compare the distinct conceptual models and validate related computational models comparing their performance to the best achievable performance. The benefits of this comparison are twofold. First, this evaluates the strengths and weaknesses of competing modeling concepts. Second, the predictive ability of each computational model is assessed. In terms of validation, we can define a hypothesis as to whether the models can satisfactorily represent the real system of interest,

provided by the pore-scale resolved model, described in Section 2.1. Furthermore, we update the prior belief in the predictive capability of the models based on Bayesian notions. The resulting so-called posterior belief is expressed in terms of probabilities. The Bayesian approach in the task of validation allows us to include possible sources of errors that can lead to inevitable uncertainties. The Bayesian validation framework requires propagation of the parametric uncertainty through the given computationally demanding models. This propagation renders the analysis intractable, as it demands a large number of model evaluations. To circumvent this problem, we employ a surrogate modeling technique to speed up the computation.

### 3.1 Bayesian Model Comparison

The topic of quantitative model comparison has received and continues to receive considerable attention in the field of statistics. There exist several multi-model comparison frameworks related to these model rating methods and allow for statistical model selection and averaging (see for example Gelman et al. (2013)). The most common approach is Bayesian model selection (BMS) (Draper, 1995; Hoeting et al., 1999). The BMS is grounded on Bayes’ theorem, which combines a prior belief about the efficacy of each model with its performance in replicating a common observation data set. Its procedure for model comparison entails principled and general solutions to the trade-off between parsimony and goodness-of-fit. Moreover, BMS is a formal statistical approach that allows comparing alternative conceptual models, testing their adequacy, combining their predictions into a more robust output estimate, and quantifying conceptual uncertainty’s contribution to the overall prediction uncertainty. BMS can be regarded as a Bayesian hypothesis testing framework, combining the idea of classical hypothesis testing with the ability to examine multiple alternative models against each other in a probabilistic manner. It returns the so-called model weights (Geman et al., 1992) representing posterior probabilities for each model to be the most appropriate one from the set of proposed competing models. Thus, the computed model weights provide a quantitative ranking for the competing conceptual models.

Let us consider  $N_m$  competing computational models  $M_k$ , each with an uncertain parameter vector of  $\theta_k$  of length  $N_k$ , yielding a quantity of interest  $Q$  in a physical space of  $x$ ,  $y$  and  $z$  and for a time stamp of  $t$ . The model weights are given by Bayes’ theorem, which can be cast for a set of  $M_k$  competing models as

$$P(M_k|\mathcal{Y}) = \frac{p(\mathcal{Y}|M_k)P(M_k)}{\sum_{i=1}^{N_m} p(\mathcal{Y}|M_i)P(M_i)}, \quad (18)$$

where  $P(M_k)$  denotes the prior probability of the model, also known as the subjective credibility that model  $M_k$  could be the the most plausible model in the set of models *before* any comparison with observed data have been made. The term  $p(\mathcal{Y}|M_k)$  is the Bayesian model evidence (BME), also known as marginal likelihood, of the model  $M_k$ . Bayes’ theorem closely follows the principle of parsimony or Occam’s razor (Angluin & Smith, 1983), in that the posterior model weights  $P(M_k|\mathcal{Y})$  offer a compromise between model complexity and goodness of fit, known as the bias-variance trade-off (Geman et al., 1992). The model weights,  $P(M_k|\mathcal{Y})$ , can be interpreted as the Bayesian probability of the individual models to be the best representation of the system from the pool of competing models.

The paper (Hoeting et al., 1999) propose that a “reasonable, neutral choice” could be equally likely priors, i.e.  $P(M_k) = 1/N_m$ , in case of paucity of prior knowledge regarding the merit of the different models under study. The denominator in equation (18) is the normalizing constant of the posterior distribution of the models and can simply be obtained by determination of the individual weights. Since all model weights are normalized by the same constant, this normalizing factor could even be neglected. Thus, the weights  $P(M_k|\mathcal{Y})$  of the individual model  $M_k$  against other models can be



**Table 1.** Interpretation of Bayes Factor in favor of model  $M_K$  according to (Jeffreys, 1961).

$\log_{10}(BF)$	Interpretation
1 - 3	anecdotal evidence
3 - 10	substantial evidence
10 - 100	strong evidence
> 100	decisive evidence

represented by the proportionality

$$P(M_k|\mathcal{Y}) \propto p(\mathcal{Y}|M_k)P(M_k). \quad (19)$$

The BME term  $p(\mathcal{Y}|M_k)$  quantifies the likelihood of the observed data based on the prior distribution of the parameters. It can be computed by integrating the likelihood term in Bayesian theorem (Kass & Raftery, 1995) over the parameter space  $\Theta_k$  of the model  $M_k$ :

$$p(\mathcal{Y}|M_k) = \int_{\Theta_k} p(\mathcal{Y}|M_k, \theta_k)P(\theta_k|M_k)d\theta_k, \quad (20)$$

with  $\theta_k$  being the parameter vector from the parameter space  $\Theta_k$  of model  $M_k$  with the dimension of  $N_{p,k}$ . The term  $P(\theta_k|M_k)$  is the corresponding prior distribution of parameters  $\theta_k$  for the model  $M_k$ . The likelihood or probability of the parameter set  $\theta_k$  of model  $M_k$  to have generated the observation data with the independent realization of  $\mathcal{Y} = (\mathcal{Y}_1, \dots, \mathcal{Y}_N)^\top$  is represented by

$$\begin{aligned} p(\mathcal{Y}|M_k, \theta_k) &:= \prod_{i=1}^N p(\mathcal{Y}_i|M_k, \theta_k) \\ &= \frac{1}{\sqrt{(2\pi)^N \det \Sigma}} \exp \left( -\frac{1}{2} (M_k(\theta_k) - \mathcal{Y})^T \Sigma^{-1} (M_k(\theta_k) - \mathcal{Y}) \right), \end{aligned} \quad (21)$$

where  $\Sigma$  denotes the covariance matrix, which includes the all error sources to be explained in Section 4.2. To obtain the BME values for each competing models, we will estimate the integral in (20) using a brute-force Monte-Carlo integration (Smith & Gelfand, 1992) avoiding unnecessary assumptions. For more details on the properties of BME and a comparison of various techniques to estimate this term, the reader is referred to Schöniger et al. (2014) and Oladyshkin and Nowak (2019).

The ratio of BME values for two alternative models is defined as the Bayes factor  $BF(M_k, M_l)$ , which is a key component in Bayesian hypothesis testing framework introduced by Jeffreys (Jeffreys, 1961):

$$BF(M_k, M_l) = \frac{P(M_k|\mathcal{Y})}{P(M_l|\mathcal{Y})} \frac{P(M_l)}{P(M_k)} = \frac{p(\mathcal{Y}|M_k)}{p(\mathcal{Y}|M_l)}. \quad (22)$$

The Bayes factor  $BF(M_k, M_l)$  is regarded as a measure for significance in Bayesian hypothesis testing. It quantifies the evidence (literally, as in Bayesian model evidence) of hypothesis  $M_k$  against the null-hypothesis  $M_l$ . Stated differently, Bayes factor  $BF(M_k, M_l)$ , can be interpreted as ratio between the posterior and prior odds of model  $M_k$  being the more plausible one in comparison to the alternative model  $M_l$  (Kass & Raftery, 1995). Jeffreys provided a rule of thumb in his book, Theory of probability (Jeffreys, 1961) for the interpretation of Bayes factor values on a log 10-scale. The grades of evidence is summarized in Table 1. Following this suggestion, a Bayes factor which lies between 1 and 3 indicates an evidence in favor of  $M_k$  that is “not worth

more than a bare mention”, a factor of up to 10 represents “substantial” evidence, and a factor between 10 and 100 can be regarded a “strong” evidence. Finally, a Bayes factor greater than 100 admits “decisive” evidence, i.e., it can be used as a threshold to reject models based on poor performance in comparison to the best performing model in the set.

### 3.2 Accelerating the Analysis via Surrogate Modeling

Bayesian validation framework requires uncertainty propagation through each competing model, demanding a significant number of model evaluations to yield statistical convergence. In practice, however, the computational complexity of the underlying computational models and the total available computational budget severely restrict the number of evaluations that one can carry out. In such situations, the Bayesian analysis estimations lack sufficient trust, as the limited number of model evaluations can yield additional uncertainty. To tackle this challenge, we replace each competing model’s behavior in the Bayesian validation framework with its easy-to-evaluate surrogate representation using the theory of polynomial chaos expansion (PCE) introduced by Wiener (1938).

The PCE representation of the model  $M_k$  provides the dependence of the computational model  $M_k$  on uncertain model’s parameters  $\theta_k$  using projection onto an orthonormal polynomial basis (Oladyshkin & Nowak, 2018). It could be also seen as a linear regression that includes linear combinations of a fixed set of nonlinear functions with respect to the input variables, known as polynomial basis function

$$M_k(x, y, z, t, \theta_k) \approx \sum_{\alpha \in \mathcal{A}} c_{\alpha}(x, y, z, t) \Psi_{\alpha}(\theta_k), \quad (23)$$

where  $x, y, z, t$  are the spatial and temporal components of the quantity of interest,  $\theta_k$  is the vector of the  $N_k$  uncertain parameters of models  $M_k$ ,  $c_{\alpha}(x, y, z, t) \in \mathbb{R}$  are the corresponding expansion coefficients that are functions of space  $x, y, z$  and time  $t$  and  $\Psi_{\alpha}(\theta_k)$  represents multivariate polynomials orthogonal with respect to a multi-index  $\alpha$ . The multi-index  $\alpha$  represents the combinatoric information how to enumerate all possible products of  $N_k$  individual univariate basis functions with respect to the total degree of expansions less or equal to  $d$  (Marelli & Sudret, 2015):

$$\begin{aligned} \mathcal{A}^{N_k, d} &= \{\alpha \in \mathbb{N}_k^N : |\alpha| \leq d\} \\ \text{card } \mathcal{A}^{N_k, d} &\equiv P = \binom{N_k + d}{d}. \end{aligned} \quad (24)$$

The multivariate polynomials  $\Psi_{\alpha}(\theta_k)$  are comprised of the tensor product of univariate polynomials

$$\Psi_{\alpha}(\theta_k) := \prod_{i=1}^{N_k} \psi_{\alpha_i}^{(i)}(\theta_{k,i}), \quad (25)$$

where the univariate orthonormal polynomials  $\psi_{\alpha_i}^{(i)}(\theta_{k,i})$  must satisfy the following

$$\langle \psi_j^{(i)}(\theta_{k,i}), \psi_l^{(i)}(\theta_{k,i}) \rangle := \int_{\Theta_{k,i}} \psi_j^{(i)}(\theta_{k,i}) \psi_l^{(i)}(\theta_{k,i}) f_{\Theta_{k,i}}(\theta_{k,i}) d\theta_{k,i} = \delta_{jl}. \quad (26)$$

where  $i$  represents the input variable with respect to which they are orthogonal as well as the corresponding polynomial family,  $j$  and  $l$  the corresponding polynomial degree,  $f_{\Theta_{k,i}}(\theta_{k,i})$  is the  $i$ th-input marginal distribution and  $\delta_{jl}$  is the Kronecker delta. We use an arbitrary polynomial chaos expansion (aPCE), introduced by Oladyshkin and Nowak (2012), that can operate with probability measures that may be implicitly and incompletely defined via their statistical moments. Using aPCE, one can build the multivariate orthonormal polynomials even in the absence of the exact probability density function  $f_{\Theta_k}(\theta)$ .

The main task of surrogate representation of the model  $M_k(x, y, z, t, \theta_k)$  in equation (23) is to compute the coefficients  $c_{\alpha}$ . However, not all coefficients could be relevant for such a surrogate. Therefore, we employ the Bayesian sparse learning method (Tipping, 2001) using a fast marginal likelihood maximization algorithm (Tipping et al., 2003). Doing so, we sequentially identify the relevant predictors (expansion terms) that capture the most significant features of the physical model. We denote this extension of aPCE as Bayesian sparse arbitrary polynomial chaos (BsPCE) representation (Mohammadi, 2020). The posterior distribution of the expansion coefficients, conditioned on the model responses  $\mathbf{Y}$  resulting from the training sets  $\mathbf{X}$ , is given by combining the a Gaussian likelihood and a Gaussian prior distribution over the unknown expansion coefficients  $\mathbf{c}$  according to Bayes' rule. Then, the posterior of the expansion coefficients given the model responses  $\mathbf{Y}$  and values of hyper-parameters  $\alpha$  and  $\beta$  describing the Gauss process (Oladyshkin et al., 2020), can take the following form

$$p(\mathbf{c}|\mathbf{Y}, \alpha, \beta) = \frac{p(\mathbf{Y}|\mathbf{X}, \mathbf{c}, \beta)p(\mathbf{c}|\alpha)}{p(\mathbf{Y}|\mathbf{X}, \alpha, \beta)}, \quad (27)$$

which is also Gaussian  $\mathcal{N}(\mathbf{c}|\mu, \Sigma)$  with

$$\begin{aligned} \mu &= \beta \Sigma \Psi^\top \mathbf{Y} \\ \Sigma &= (\mathbf{A} + \Psi^\top \beta \Psi)^{-1}, \end{aligned} \quad (28)$$

where  $\Psi$  is the design matrix of the size  $E \times N$  with elements  $\Psi_{ni} = \psi_i(x_n)$ , and  $\mathbf{A} = \text{diag}(\alpha_i)$ . Here,  $E$  represents the number of model evaluations using the training samples. The values of  $\alpha$  and  $\beta$  can be determined via type-II maximum likelihood (Berger, 2013). Having found values  $\alpha^*$  and  $\beta^*$  for the hyperparameters that maximize the marginal likelihood, one can evaluate the predictive distribution over  $Y$  for a new input  $\mathbf{x}$  by

$$\begin{aligned} p(Y|\mathbf{x}, \mathbf{X}, \mathbf{Y}, \alpha^*, \beta^*) &= \int p(Y|\mathbf{x}, \mathbf{c}, \beta^*)p(\mathbf{c}|\mathbf{X}, \mathbf{Y}, \alpha^*, \beta^*)d\mathbf{c} \\ &= \mathcal{N}(Y|\mu^\top \Psi(\mathbf{x}), \sigma^2(\mathbf{x})). \end{aligned} \quad (29)$$

The predictive mean is given by (28) with  $\mathbf{c}$  set to the posterior mean  $\mu$ , and the variance of the predictive distribution is given by

$$\sigma^2(\mathbf{x}) = (\beta^*)^{-1} + \Psi(\mathbf{x})^\top \Sigma \Psi(\mathbf{x}) \quad (30)$$

where  $\Sigma$  is calculated by Equation (28) in which  $\alpha$  and  $\beta$  set to their optimized values  $\alpha^*$  and  $\beta^*$ . For the latter, a separate hyper-parameter  $\alpha_i$  is assigned to each weight parameter  $c_i$ .

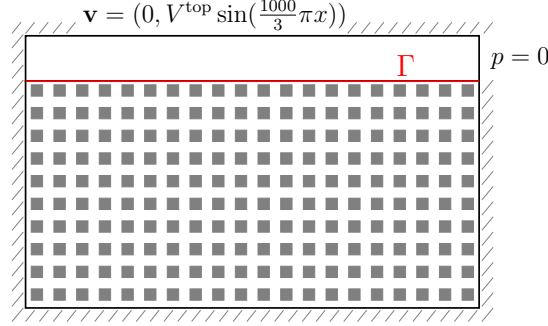
## 4 Benchmark Scenario

Corresponding to Figure 1, we investigate rectangular solid inclusions of size  $d$  and consider a flow problem where the flow is not only parallel but also arbitrary to the fluid-porous interface  $\Gamma$ . We describe the geometrical configuration and the boundary conditions in Section 4.1, followed by a description of the uncertainties in Section 4.2 and the system response quantities in Section 4.3.

### 4.1 Geometrical Setting and Boundary Conditions

We consider the free-flow region  $\Omega_{\text{ff}} = (0, L) \times (\gamma, H)$  and the porous-medium domain  $\Omega_{\text{pm}} = (0, L) \times (0, \gamma)$  with  $L = 10.25$  mm and  $H = 6$  mm, separated by the sharp fluid-porous interface  $\Gamma$ , where the exact value for  $\gamma$  is uncertain. The porous medium is isotropic,  $\mathbf{K} = k\mathbf{I}$ , and consists of  $20 \times 10$  square solid inclusions of size  $d = 0.25$  mm (Figure 4). The inclusions are positioned in such a way that

the equation of the line tangent to the top of the upper row of solid inclusions is given by  $(0, L) \times \{4.975 \text{ mm}\}$ . The characteristic pore size  $\ell$  appearing in the coupling condition (12) is  $\ell = 0.5 \text{ mm}$ .

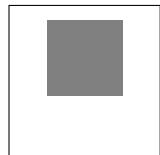


**Figure 4.** Schematic description of the coupled flow problem.

For the interface conditions (7)–(9) (*Classical IC*) the Beavers–Joseph parameter is typically taken  $\alpha_{\text{BJ}} = 1$  in the literature, although it is often not the optimal choice (Rybak et al., 2021). Here, we consider  $\alpha_{\text{BJ}}$  as an uncertain parameter, which will be quantified in Sections 4.2 and 4.3. The permeability values and the boundary layer constants appearing in the coupling conditions (10)–(12) are computed numerically based on the pore geometry and presented in Table 2. For details on the computation of these effective parameters, we refer the reader to (Eggenweiler & Rybak, 2021).

Note that the permeability values and the boundary layer constants presented in Table 2 are non-dimensional. In order to obtain the effective physical permeability  $k$ , we scale it accordingly to  $k = \ell^2 \tilde{k}$ . For example, for the pore geometry presented in Table 2 (left), we obtain  $k = 3.25 \times 10^{-9} \text{ m}^2$ . For isotropic porous media, the constants  $M_1^{2,\text{bl}} = 0$  and  $N_s^{\text{bl}} = 0$ , therefore, they do not appear in Table 2.

**Table 2.** Non-dimensional effective properties for the interface location  $\gamma = 5 \text{ mm}$ ,  $k = \ell^2 \tilde{k}$ .

	$\tilde{k}$	$1.30 \times 10^{-2}$
	$N_1^{\text{bl}}$	$-1.18 \times 10^{-1}$
	$M_1^{1,\text{bl}}$	$-7.16 \times 10^{-3}$

In order to obtain a closed formulation for the pore-scale problem (1), (2) we set the following boundary conditions on the external boundary

$$\mathbf{v} = (0, V^{\text{top}} \sin(\frac{1000}{3} \pi x)) \quad \text{on } \Gamma_{\text{in}}, \quad (31)$$

$$\frac{\partial \mathbf{v}}{\partial x} = 0, \quad p = 0 \quad \text{on } \Gamma_{\text{out}}, \quad (32)$$

$$\mathbf{v} = (0, 0) \quad \text{on } \Gamma_{\text{nf}}, \quad (33)$$

where  $\Gamma_{\text{in}} = (3 \text{ mm}, 6 \text{ mm}) \times \{H\}$ ,  $\Gamma_{\text{out}} = \{L\} \times (\gamma, H)$  and  $\Gamma_{\text{nf}} = \partial\Omega \setminus (\Gamma_{\text{in}} \cup \Gamma_{\text{out}})$ . The boundary conditions for the coupled flow problem are presented schematically in Figure 4.

The corresponding boundary conditions for the macroscale model formulation given by (3)–(4) together with either the *Classical IC* (7)–(9) or the *Generalized IC* (10)–(12), which are valid for arbitrary flow directions, read

$$\mathbf{v}_{\text{ff}} = (0, V^{\text{top}} \sin(\frac{1000}{3}\pi x)) \quad \text{on } \Gamma_{\text{in}}, \quad (34)$$

$$\frac{\partial \mathbf{v}_{\text{ff}}}{\partial x} = 0, \quad p_{\text{ff}} = 0 \quad \text{on } \Gamma_{\text{out}}, \quad (35)$$

$$\mathbf{v}_{\text{ff}} = (0, 0) \quad \text{on } \Gamma_{\text{nf,ff}}, \quad (36)$$

$$\mathbf{v}_{\text{pm}} \cdot \mathbf{n} = (0, 0) \quad \text{on } \Gamma_{\text{nf,pm}}, \quad (37)$$

where  $\Gamma_{\text{nf,ff}} = \partial\Omega_{\text{ff}} \setminus (\Gamma_{\text{in}} \cup \Gamma_{\text{out}} \cup \Gamma)$ ,  $\Gamma_{\text{nf,pm}} = \partial\Omega_{\text{pm}} \setminus \Gamma$  and  $\mathbf{n}$  denotes the unit normal vector on  $\partial\Omega_{\text{pm}}$  pointing outward the porous medium.

The boundary conditions (34)–(36) also hold for the hybrid-dimensional free-flow/pore-network model such that no mass enters or leaves the domain through the pores on  $\Gamma_{\text{nf,pm}}$ . The coupling conditions (13)–(15) are set on  $\Gamma$ .

## 4.2 Uncertainties and Errors

So far, we have presented various coupling concepts for free flow and porous-medium flow. These concepts only differ in the description of processes in the porous medium, where different mathematical models are employed, whereas the free flow for all concepts is modeled based on the standard Stokes equations. The uncertainty due to the choice of the adequate representation of the system of interest is known as conceptual uncertainty. In addition to the conceptual uncertainty, each computational model includes uncertain parameters, such as upscaling parameters, material parameters, or interface location, requiring a thorough investigation. This uncertainty is known as parametric uncertainty. Uncertain model inputs have to be propagated through the model or simulation (also known as uncertainty propagation) to effectively assess competing modeling concepts’ response quantities and validate the corresponding computational models against a reference solution.

Regarding the classical coupled Stokes–Darcy model, the benchmark scenario contains four uncertain parameters: the maximum boundary velocity at the opening, the exact interface position, the Beavers–Joseph coefficient, and the permeability tensor. We refer to Section 1 for a brief literature overview on the role of these model parameters. In contrast to the *Classical IC*, the *Generalized IC* don’t require the Beavers–Joseph coefficient and also rely on the assumption that the interface location may not be below the top of the solid inclusions. Correspondingly, the parameters and their associated distributions as prior knowledge for the Stokes–Darcy model with the *Classical IC* and the *Generalized IC* are listed in Table 3 and Table 4, respectively.

As for the *pore-network* model, the throat conductance  $g_{t,ij}$  in (6) can be described by a numerical upscaling technique (Mehmani & Tchelepi, 2017; Weishaupt

**Table 3.** The uncertain parameters and their associated distribution for the classical coupled Stokes–Darcy model.

Parameter name	Range	Unit	Distribution type
Boundary velocity, $V^{\text{top}}$	$[10^{-4}, 10^{-2}]$	m/s	uniform
Beavers–Joseph parameter, $\alpha_{\text{BJ}}$	$[0, 10]$	-	uniform
Exact interface location, $\Gamma$	$[4.75, 5.125]$	mm	uniform
Permeability, $\mathbf{K}$	$[10^{-10}, 10^{-7}]$	m <sup>2</sup>	log normal

**Table 4.** The uncertain parameters and their associated distribution for the Stokes–Darcy model with the generalized interface conditions.

Parameter name	Range	Unit	Distribution type
Boundary velocity, $V^{\text{top}}$	$[10^{-4}, 10^{-2}]$	m/s	uniform
Exact interface location, $\Gamma$	$[4.975, 5.125]$	mm	uniform
Permeability, $\mathbf{K}$	$[10^{-10}, 10^{-7}]$	m <sup>2</sup>	log normal

et al., 2019). We consider this parameter and its counterpart  $g_{p,i}$  for a half pore (see Figure 2) as uncertain parameters to be inferred during the calibration phase. The third uncertain input parameter is the pore-scale slip coefficient  $\beta_{\text{pore}}$ . It can be determined numerically in a preprocessing step, in which it is approximated by solving a simplified, equivalent problem of free flow over a single pore throat intersecting with the lower boundary of the free-flow channel (Weishaupt et al., 2020). The list of considered uncertain parameters and their associated distribution as prior knowledge for the PNM model are presented in Table 5.

**Table 5.** The uncertain parameters and their specifications for the pore-network model.

Parameter name	Range	Unit	Distribution type
Boundary velocity, $V^{\text{top}}$	$[10^{-4}, 10^{-2}]$	m/s	uniform
Conductance of throats, $g_{t,ij}$	$[10^{-7}, 10^{-4}]$	m <sup>3</sup> /(s · Pa)	uniform
Conductance of half pores, $g_{p,i}$	$[10^{-7}, 10^{-4}]$	m <sup>3</sup> /(s · Pa)	uniform
Pore-local slip coefficient, $\beta_{\text{pore}}$	$[10^3, 10^5]$	1/m	uniform

As opposed to uncertainties, errors are defined as the difference between the true value and the predicted value, and have both a sign and a magnitude. We will consider the errors associated with the conceptual observation error, numerical approximation, and surrogate modeling in our analysis.

*Conceptual observation error.* In the current benchmark case study, we have a fully resolved pore-scale solution as a reference. However, in practice, the reference solution is not available, and instead, experimental data should be incorporated that includes an observation error. However, the analyzed models in our benchmark study could contain a conceptual error due to the scale difference compared to the pore-scale reference solution. Therefore, we will consider a conceptual observation error to simulate an observation error from a possible experimental setup and incorporate a conceptual modeling error.

*Numerical error.* The governing equations of the models under investigation in this study require approximation of the numerical solutions. These approximations provide an additional source of error. There are five primary sources of errors in computational physics solutions, given that the numerical scheme is stable, consistent, and robust. These sources are insufficient spatial discretization, insufficient temporal discretization, insufficient iterative convergence, computer round-off, and computer programming (Roy, 2019). Since quantifying errors from these sources is the main focus in the verification of numerical schemes, we only investigate the discretization error that originates from a certain choice of the mesh size. Following Oberkampf and Roy (2010), we take a heuristic approach to quantify this error, in that we fit

generalized Richardson extrapolation to estimate the error by comparing three different mesh spacings. The Richardson extrapolation takes the following form

$$f_k = \bar{f} + g_p h_k^{\hat{p}} + \mathcal{O}(h_k^{\hat{p}+1}), \quad (38)$$

where  $f_k$  denotes the exact solution to the discrete equation on a mesh with a known spacing  $h_k$ ,  $\bar{f}$  stands for the exact solution to the original PDE (unknown).  $g_p$  is the error term coefficient, and  $\hat{p}$  indicates the observed order of accuracy. Here, we seek the first-order error. Thus, the unknowns  $\bar{f}$  and  $g_p$  can be easily determined via the least square method for the numerical solutions obtained by varying the mesh spacing.

*Surrogate error.* As previously mentioned, we substitute the computational models with the easy-to-evaluate surrogate models in the Bayesian analysis to offset the computational cost. This replacement also introduces a new source of error, known as a surrogate prediction error. Ignoring this error could result in a biased posterior distribution. As for prediction uncertainty, a mean squared error based on a testing set can provide a good estimate of the surrogate error variance.

We will incorporate the errors discussed above in the Markov Chain Monte Carlo (MCMC) simulation method to approximate the posterior distribution (Robert & Casella, 2013; Liu, 2008), used in the calibration stage. We directly sum up all the covariance matrices of errors to obtain the likelihood calculations' total covariance matrix. Here, we assume that all these errors follow a normal distribution and are independent.

### 4.3 System Response Quantities

A fundamental ingredient of each benchmark is the definition of so-called system response quantities (SRQs) which define the prescribed output from the reference/experimental data as well as from the computational models that is to be compared in terms of the validation metric. The SRQs can be either local or global quantities. While the former can take quantities within the solution domain on the PDEs, such as dependent variables of the PDEs, the latter represents integral quantities, e.g., or net flux out of a system. As part of model validation, we seek to compare system responses generated by different coupling concepts with the ones from the pore-scale resolved model (Section 2.1).

Figure 5 shows the data extraction points for the velocity field (left) and the pressure (right). We will train the surrogate models for all computational models based on the simulation results for the marked points. The points colored in blue and red provide the corresponding data for the calibration and validation steps, respectively.

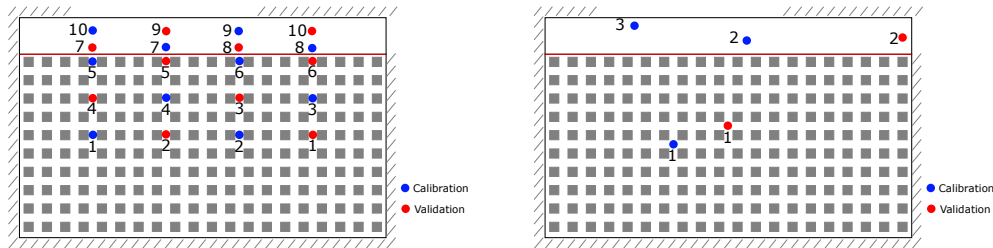


**Figure 5.** Data extraction points for the velocity field (left) and pressure (right) for the calibration and validation scenarios.

The pore-scale resolved simulation results contain both macroscopic and micro-scope details of the flow field. The latter become visible as oscillations of the pore-

scale solutions in the porous medium. In order to make a comparison of microscale and macroscale numerical simulation results, the pore-scale solutions need to be averaged. We consider volume averaging, where the averaged velocity field at a given point  $\mathbf{x}_0 \in \Omega$  is obtained as

$$\mathbf{v}_{\text{avg}}(\mathbf{x}_0) = \frac{1}{|V(\mathbf{x}_0)|} \int_{V_f(\mathbf{x}_0)} \mathbf{v}(\mathbf{x}) d\mathbf{x}, \quad (39)$$

where  $V(\mathbf{x}_0)$  is the representative elementary volume corresponding to  $\mathbf{x}_0$  and  $V_f(\mathbf{x}_0)$  is its fluid part. The representative elementary volume  $V(\mathbf{x}_0)$  has the same size as the periodicity cell  $Y^\ell$ . Moreover, also the simulation results need to be averaged correspondingly such that the interpretation of the SRQs is the same in all cases.

## 5 Application of the Bayesian Framework

In this section, we compare the coupled models (using either a macro-scale formulation or the *pore-network* model in  $\Omega_{\text{pm}}$ ) with the pore-scale resolved model (1), (2). For the macro-scale model formulation, we consider the Stokes–Darcy problem with the *Classical IC* (7)–(9) and the coupling conditions for arbitrary flows (10)–(12). We demonstrate that the *Generalized IC* (10)–(12) are more accurate than the *Classical IC* for parallel flows to the interface and suitable for arbitrary flow directions where the *Classical IC* fail. As shown in Weishaupt et al. (2019, 2020), the hybrid-dimensional coupled model using a *pore-network* approach in  $\Omega_{\text{pm}}$  can be an efficient and accurate choice for simulating free flow over structured porous media. Here, our goal is to assess the coupled model’s accuracy in comparison to the above-mentioned REV-scale approaches and under the influence of pore-scale parameter uncertainty. As a reference data we will use the fully resolved fully resolved data pore-scale model for velocity field and pressure profile according to Figure 5. However, it is worth mentioning that the Stokes–Darcy model with *Classical IC* and *Generalized IC* can only offer predictions on the REV scale. Therefore, we will average the values of SRQs obtained for the fully resolved pore-scale model and as well as the *pore-network model* for consistency. The averaging is performed via a volume averaging approach, discussed in Section 4.3 to make the macroscale numerical simulation results comparable with that of the pore-scale resolved simulation. The current section offers insights on analysis of predictive abilities in Section 5.2 and model comparison in Section 5.3 using the introduced surrogate-based Bayesian validation framework in Section 3. Additionally, we also assess the influence of various modeling parameters onto the final model prediction, performing the global sensitivity analysis in Section 5.1.

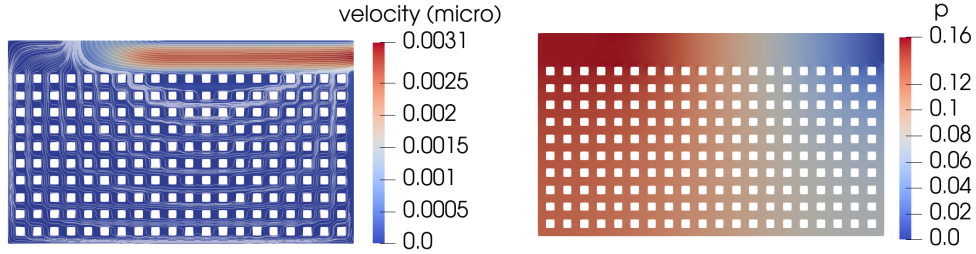


**Figure 6.** Streamlines of the pore-scale velocity field (left) and pressure profile (right).

### 5.1 Global Sensitivity Analysis

In this section, we analyze how the variability of the model response quantities, introduced in Section 4.3, at the selected data extraction points (Figure 5), is affected



by the variability of each input variable or combinations thereof. This can be achieved via a sensitivity analysis. Various sensitivity analysis approaches have been developed in the recent years. For an extensive review of different techniques, see Iooss and Lemaître (2015). In the current paper, we explore the connection of polynomial representation to a global sensitivity measures (Oladyshkin et al., 2012) and use the so-called *Sobol indices* (Sobol', 1993), derived from a variance decomposition of model outputs in terms of contributions of each input parameter or combinations thereof. Using Sobol decomposition, one can describe the total variance of the model in terms of the sum of the summands' variances. This variance decomposition is extensively explained in Sudret (2008). Leveraging the orthonormality of the polynomial chaos basis, the authors also derive so-called PC-based Sobol indices. The idea behind these indices is as follows: once the PC representation of the model in (23) is available, the expansion coefficients  $c_\alpha$  are simply gathered according to the dependency of each basis polynomial, square-summed and normalized

$$S_{i_1, \dots, i_s} = \frac{\sum_{j=1}^M \chi_j c_j^2}{\sum_{j=1}^M c_j^2} \quad (40)$$

$$\chi_j = \begin{cases} 1, & \text{if } \alpha_j^k > 0, \quad \forall j \in (i_1, \dots, i_s) \\ 0, & \text{if } \alpha_j^k = 0, \quad \exists j \in (i_1, \dots, i_s) \end{cases},$$

where  $S_{i_1, \dots, i_s}$  is the Sobol index that indicates what fraction of total variance of the response quantity can be traced back to the joint contributions of the parameters  $\theta_{i_1}, \dots, \theta_{i_s}$ . The index selection operator  $\chi_j$  indicates where the chosen parameters  $\theta$  numbered as  $i_1, \dots, i_s$  (i.e.,  $\theta_{i_1}, \dots, \theta_{i_s}$ ) have concurrent contributions to the variance within the overall expansion. Simply put, it selects all polynomial terms with the specified combination  $i_1, \dots, i_s$  of model parameters.

A complementing measure for sensitivity analysis is the *Sobol Total Index*. It expresses the total contribution to the variance of model output due to the uncertainty of an individual parameter  $\theta_j$  in all cross-combinations with other parameters

$$S_j^T = \sum_{\{i_1, \dots, i_s\} \supset j} S_{i_1, \dots, i_s} \quad (41)$$

where  $S_j^T$  is simply a summation of all Sobol indices in which the variable  $\theta_j$  appears as univariate as well as joint influences. The Total Sobol indices sum to one, if input variables are independent. When dealing with correlated variables, however, this is not the case. In what follows, we present the total Sobol indices for the SQRs and the data extraction points defined in Section 4, for all three models for the validation scenario.

*Classical IC.* In Figure 7, we provide the total Sobol indices for the validation points in red (Figure 5) for velocity and pressure. We observe that the exact interface location plays an important role for the velocity field, especially near the interface (Figure 7, left) and influences the pressure field as well (Figure 7, right). The value of the Beavers–Joseph parameter has a significant impact on the velocity near the interface, however, does not play an essential role for the pressure. The permeability  $\mathbf{K}$  impacts both the velocity and pressure fields in the free-flow and porous-medium domains, and the most important influence has the inflow velocity  $V^{\text{top}}$ .

*Generalized IC.* In Figure 8, the total Sobol indices for velocity and pressure before calibration are presented for the selected red points in Figure 5. For the *Generalized IC*, the information about the exact interface location  $\Gamma$  is included in the boundary layer constants  $N_1^{\text{bl}}$  and  $M_1^{1, \text{bl}}$  appearing in condition (12). Therefore, the exact position of interface does not influence the overall system behavior in comparison to the *Classical IC*. The permeability  $\mathbf{K}$  and the inflow velocity  $V^{\text{top}}$  have significant impact both on the velocity and pressure fields as in the case of the *Classical IC*.

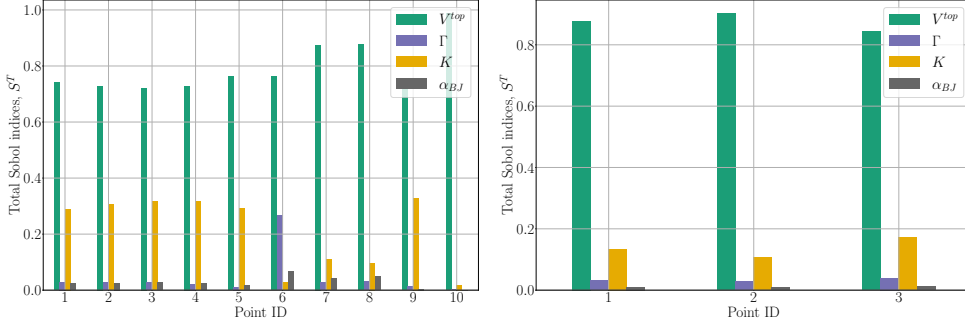


**Figure 7.** Total Sobol indices of the Stokes–Darcy model with the *Classical IC* for the velocity (left) and pressure (right) for the calibration (blue) points in Figure 5.

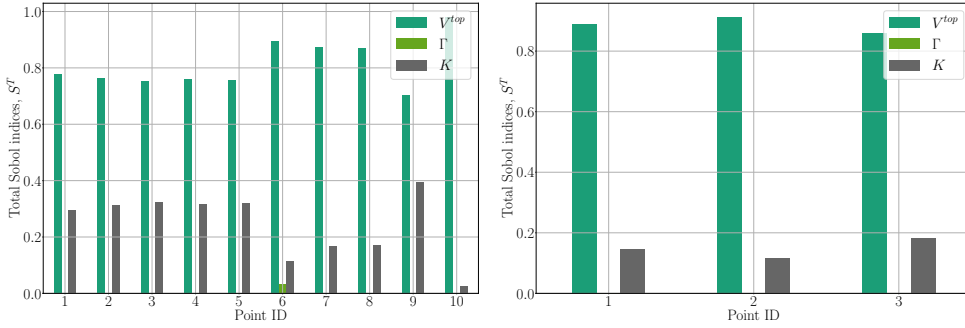


**Figure 8.** Total Sobol indices of the Stokes–Darcy model with the *Generalized IC* for the velocity (left) and pressure (right) for the calibration (blue) points in Figure 5.

*Pore-network model.* Figure 9 shows the total Sobol indices for velocity (left) and pressure (right) before calibration for the selected red points in Figure 5. As for the REV-scale coupled models, we observe a dominant influence of  $V^{top}$  for all validation points. As expected, the influence of the throat conductance ( $g_{t,ij}$ ) and the half-pore conductance ( $g_{p,i}$ ) is most prominent in the porous domain, comparable to the influence of permeability for the REV-scale coupled models. The influence of the pore-scale slip parameter  $\beta$  is only visible for location 6, and also there it is very small. This is most likely related to the fact that the slip coefficient only affects the flow field in the free-flow domain  $\Omega_{ff}$  very locally, directly above the interface pore. The averaging volume used for the evaluation, however, takes into account a larger portion of the free-flow region, where the influence of  $\beta$  is very small. In analogy to the REV models,  $V^{top}$  has also a dominating influence on the pressure.

## 5.2 Analysis of Predictive Abilities

This section presents the result of the analysis of the predictive ability of all three discussed conceptual models by showing the their parametric posterior and the corresponding predictive distributions. To pursue this goal, we follow the surrogate-based Bayesian procedure described in Section 3. In the calibration phase, we update the prior knowledge on the uncertain model parameters according to Section 4.2 conditioning the responses of all analyzed models on the velocity and pressure values extracted from the pore-scale simulations that are marked as a blue points in Figure 5. To do so, we employ MCMC approach (*emcee* Python ensemble sampling toolkit (Foreman-Mackey et al., 2019)) in order to perform Bayesian inference in Sec-

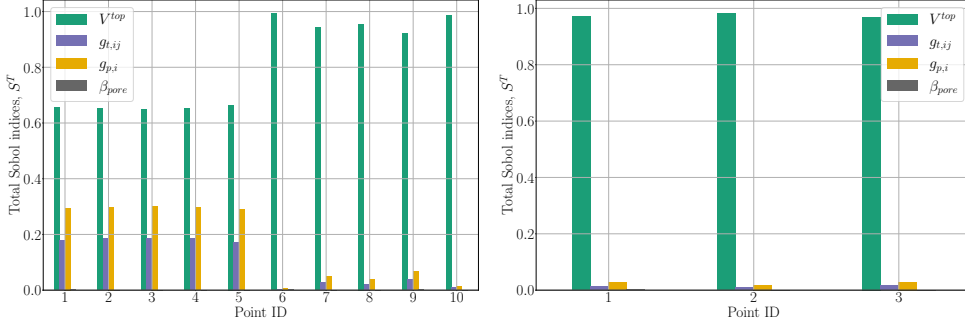


**Figure 9.** Total Sobol indices of the *pore-network* model for the velocity (left) and pressure (right) for the calibration (blue) points in Figure 5.

tion 3.1 using BsaPCE surrogate representation in Section 3.2. To accelerate this Bayesian updating step, we train each surrogate model with the simulation outcomes of 300 runs of each numerical model. The MCMC algorithm is run for an ensemble of 500 Markov chains on each surrogate. We monitor the convergence of the sampler using the integrated auto-correlation time, which estimates the number of evaluations of the posterior probability density function to draw independent samples from the target density. For more details on MCMC, we refer the reader to Goodman and Weare (2010). The MCMC sampler is run until the convergence criterion of 1% for the difference in the auto-correlation time between two consequent monitoring steps is met. In the validation stage, we retrain a new set of surrogate models based on the updated parameter distribution (posterior distribution) obtained after calibration.

As discussed in Section 4.2, using surrogates may introduce additional errors to the inference process. To include this error, we test the surrogate models with 100 simulation runs (test sets) different from the training sets. Comparing the surrogates' prediction with the results from the test sets, we estimate Mean Square Error (MSE) for each surrogate model. The MSE is a good estimate of the surrogate error variance (Xu & Valocchi, 2015). When evaluating the likelihood  $p(\mathcal{Y}|M_k, \theta_k)$  in (21), we add a diagonal matrix  $\Sigma_{\text{PCE}}$  with elements  $\sigma_{\text{PCE},i}^2 = \text{MSE}_i$ ,  $i = 1, 2, \dots, N_{\text{out}}$  to  $\Sigma$ , assuming that the surrogate errors are independent and follow a normal distribution with zero mean. Moreover, following Schöniger et al. (2015), we perturb the reference data with some additive noise to account for uncertainty associated with the BME values, the resulting Bayes factors, and posterior model weights. With this approach, we investigate the impact of other possible sources of errors on the validation metrics that are not considered in the calculations.

*Classical IC.* Figure 10 presents the posterior distribution truth Bayesian calibration procedure using the calibration (blue) points in Figure 5. The 50 percent quantiles, alongside the 15 and 85 percent quantiles, are displayed on top of the histogram in the diagonal plots. The posterior clearly follows a multivariate Gaussian distribution. Propagating these posterior parametric uncertainty (Figure 10) through the *Classical IC* model offers a possibility to analyze how the post-calibration uncertainty affects the SRQs. To do so, we have trained a new set of surrogates using the information obtained during the calibration step. Figures 11 and 12 show the posterior predictive distributions of the velocity and the pressure for the selected validation (red) points in Figure 5, respectively. The solid vertical lines in green represent the validation data set, extracted from the pore-scale simulation at the validation (red) points in Figure 5. The bars in gray at the top are the responses of the original computational model.

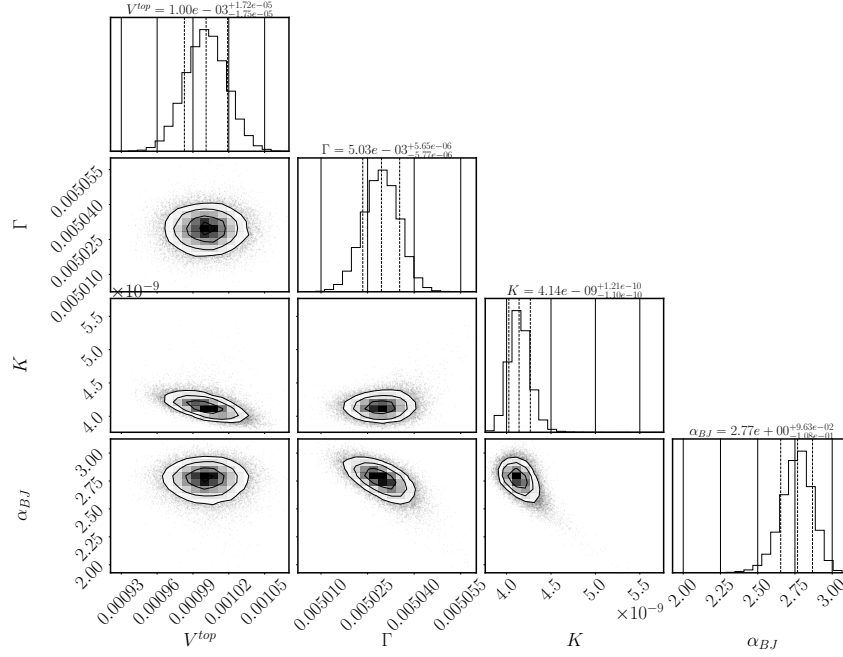


**Figure 10.** Posterior parameters distribution of the Stokes–Darcy model with the *Classical IC* after calibration to the reference data from the pore-scale model.

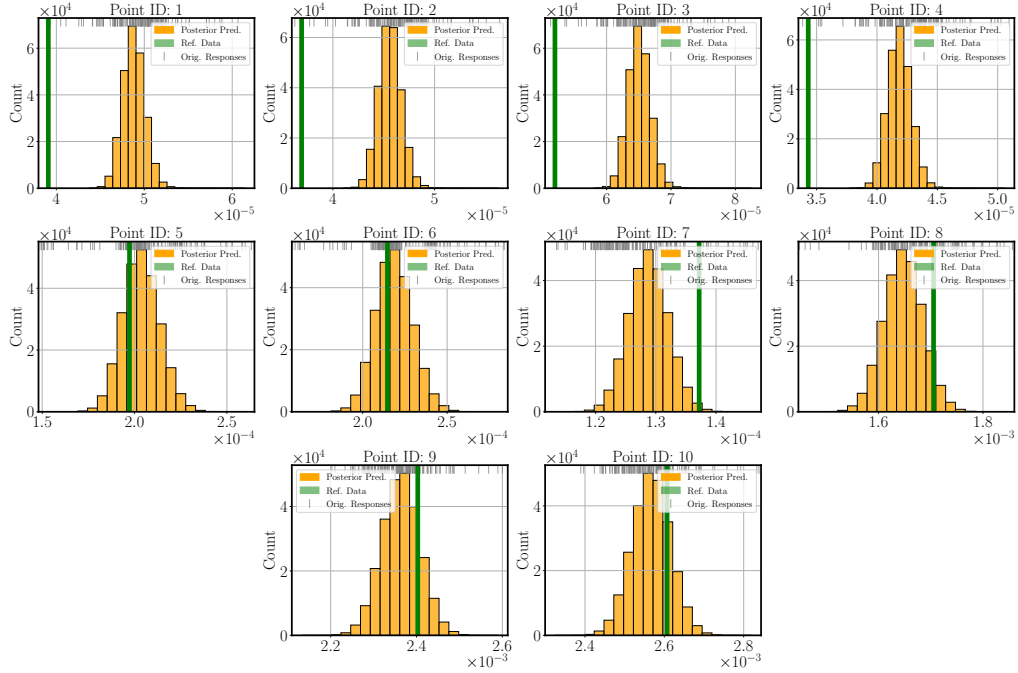


**Figure 11.** Velocity posterior distribution of the Stokes–Darcy model with the *Classical IC* in validation step against the reference data from the pore-scale model.

The plots in the first row of Figure 11 reveals that the Stokes–Darcy model with *Classical IC* shows discrepancy between the predictions and the reference velocity values in the deeper part of the porous medium. This discrepancy could be attributed

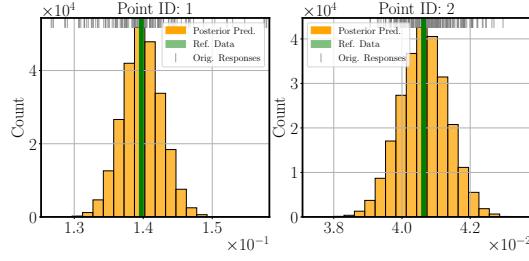


**Figure 12.** Pressure posterior distribution of the Stokes–Darcy model with the *Classical IC* in validation step against the reference data from the pore-scale model.

to the fact that the points closer to the interface and in the free flow domain received higher weights in the likelihood calculation in (21). These likelihoods are then used in the calibration via the MCMC method to approximate the posterior distribution that describes the remaining parametric uncertainty after calibration. However, *Classical IC* adequately estimates the velocity in the vicinity of the interface and the free-flow section of the domain. Moreover, the *Classical IC* model also provides reasonable pressure predictions compared to the reference data.

*Generalized IC.* Similar to the described procedure above, the surrogate-based Bayesian calibration offers insight into the posterior distributions of modeling parameters for the *Generalized IC* model in Figure 13. The posterior distribution of uncertain parameters follows a multivariate Gaussian distribution similar to the *Classical IC* model. However, propagation of the remaining posterior parametric uncertainty

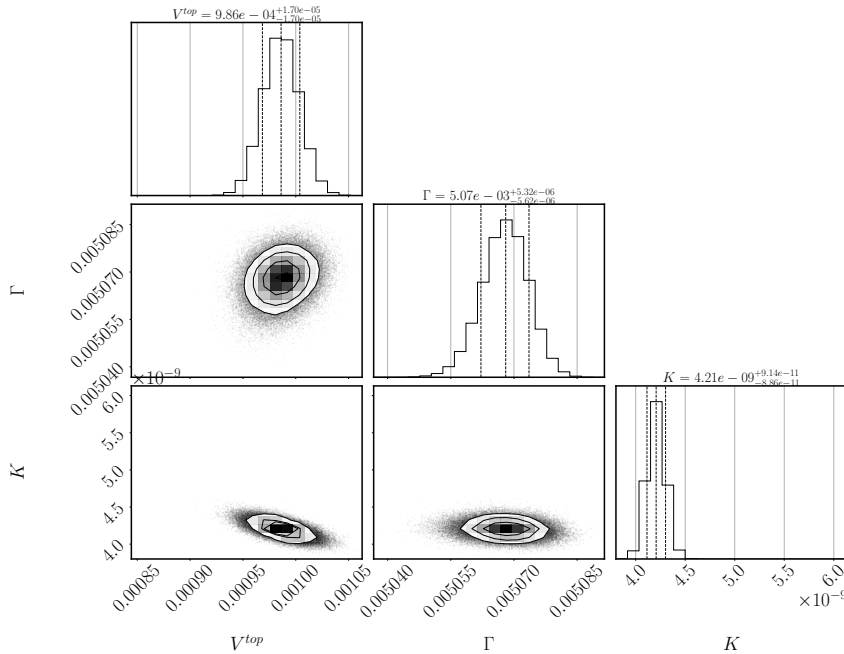


**Figure 13.** Posterior parameters distribution of the Stokes–Darcy model with the *Generalized IC* after calibration to the reference data from the pore-scale model.

through the *Generalized IC* model shows significant improvement of the prediction for SRQs during the validation phase.

Figure 14 illustrates the posterior predictive distributions of the velocity for the selected validation (red) points in Figure 5. In contrast to the *Classical IC* model, the *Generalized IC* model captures accurately the velocities located deep in the porous medium as well (points 1 to 4). Furthermore, the latter delivers fairly certain velocity estimations, suggested by narrow histograms in the second and the third rows in Figure 14. The posterior predictive distributions for the pressure are displayed in Figure 15, where *Generalized IC* model adequately represents the underlying physical processes according to the reference data from the fully resolved pore-scale model.

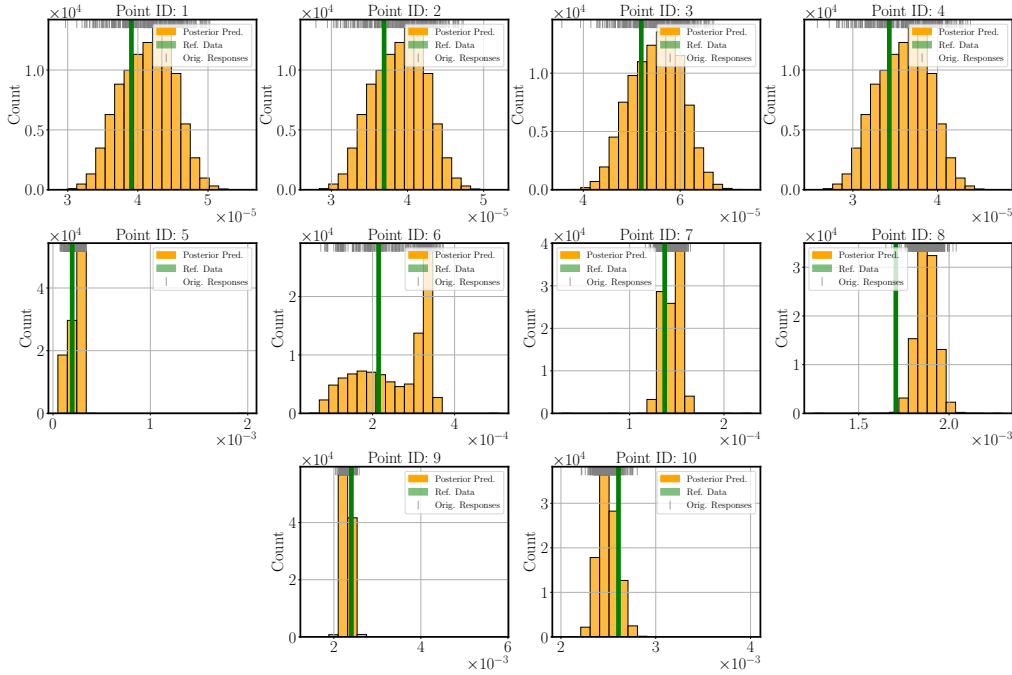


**Figure 14.** Velocity posterior distribution of the Stokes–Darcy model with the *Generalized IC* in validation step against the reference data from the pore-scale model.

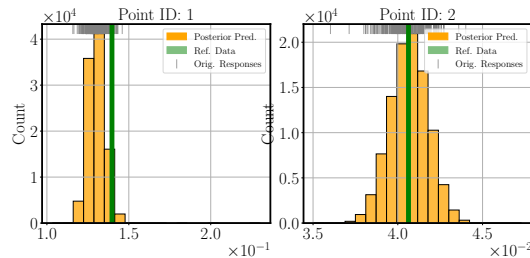


**Figure 15.** Pressure posterior distribution of the Stokes–Darcy model with the *Generalized IC* in validation step against the reference data from the pore-scale model.

*Pore-network model.* For the *pore-network* model we also have used the calibration (blue) points (Figure 5) to perform surrogate-based Bayesian inference. Figure 16

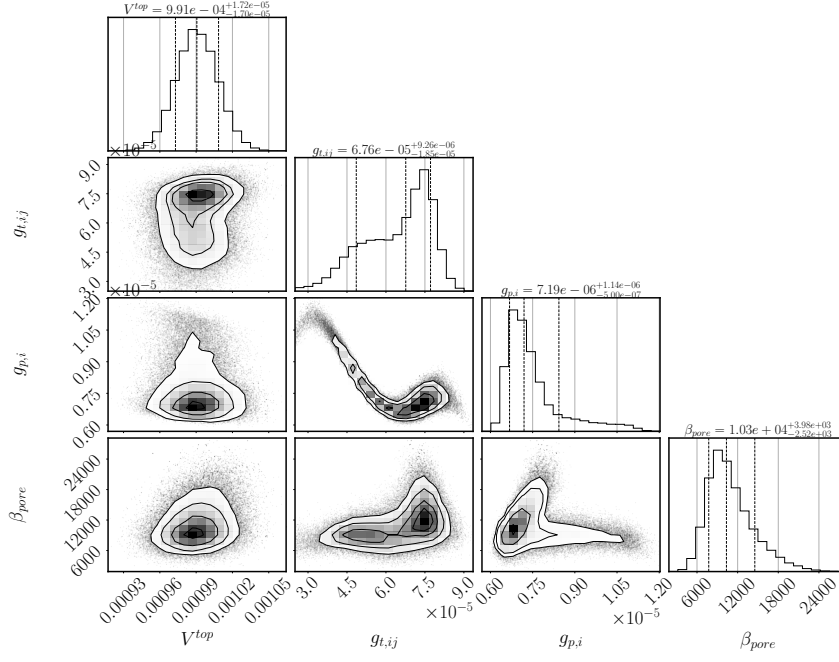


**Figure 16.** Posterior parameters distribution of the *pore-network* model after calibration to the reference data from the pore-scale model.

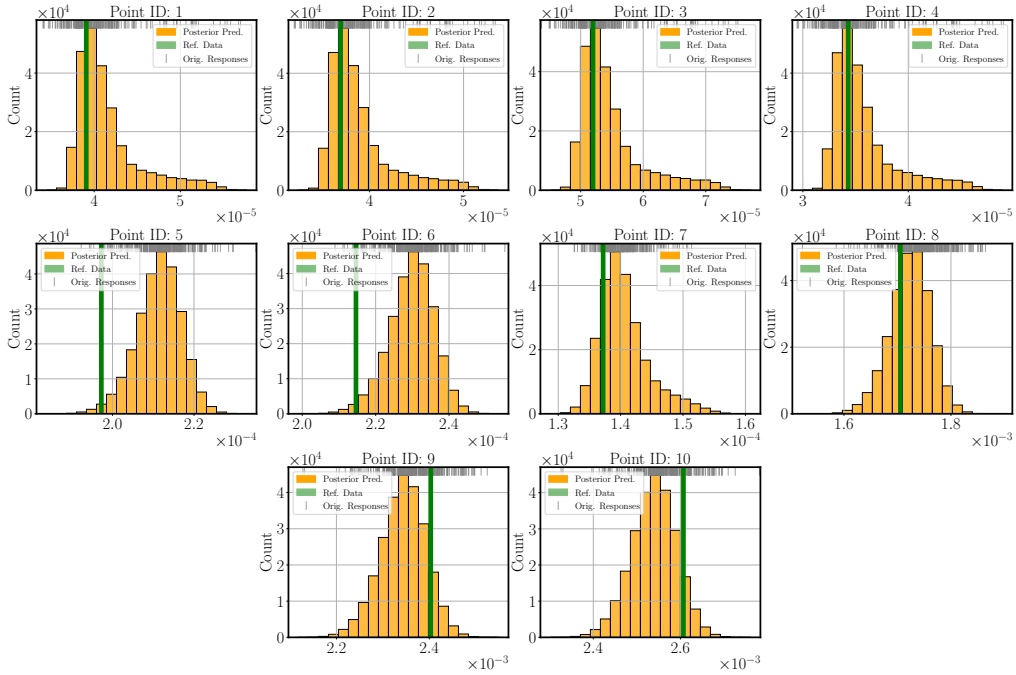


**Figure 17.** Velocity posterior distribution of the *pore-network* model in validation step against the reference data from the pore-scale model.

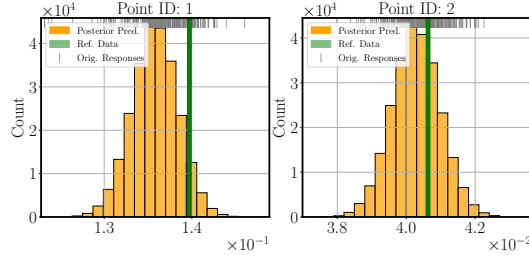


**Figure 18.** Pressure posterior distribution of the *pore-network* model in validation step against the reference data from the pore-scale model.

illustrates the posterior parameters distribution of the *pore-network*. In contrast to the *Classical IC* and *Generalized IC* models, we observe stronger non-Gaussian shapes of posteriors. Especially, the parameters  $g_{t,ij}$  and  $g_{p,i}$  are strongly dependent, as seen in Figure 16, which clearly reflects their combined contribution to the total conductance  $g_{ij}$ , see Equation (6). Propagation of the remaining post-calibration parametric uncertainty through *pore-network* model demonstrates adequate agreement with the validation data (red points in Figure 5).

The posterior predictive distributions for the velocity and the pressure are shown in Figure 17 and Figure 18, respectively. Moreover, the *pore-network* model’s velocity predictions for the points located deep in the porous medium (points 1 to 4) are more precise than for the other two modeling variants. This could be explained by the fact that the PNM preserves discrete flow paths as the throats are directly aligned with the geometry. Although the *pore-network* model approximated the reference data below and above the interface reasonably well, its velocity histograms are not as confident as that of the *Generalized IC*.

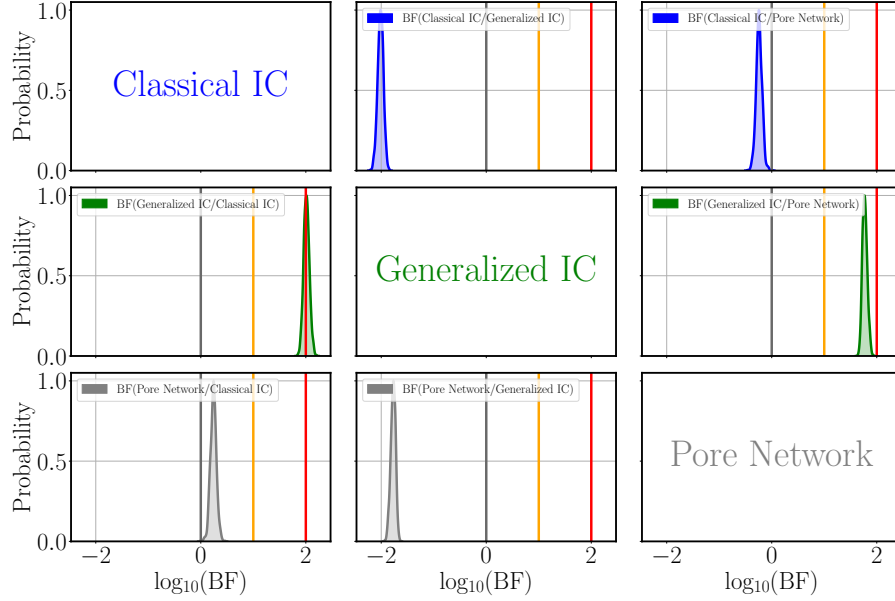
### 5.3 Model Comparison

We will perform the model comparison employing the so-called posterior model weights according to the Bayesian approach explained in Section 3.1. Such an analysis offers the aggregated comparison of model’s outputs to the validation set of reference data from the pore-scale model that are marked in red in Figure 5. For model comparison analysis, we use the newly constructed surrogate representation during the validation stage to compute the BME values in (20), the Bayes factors in (22) and the posterior model weights (18).

Assessments of confidence in model ranking have been investigated by means of Bayes factor (22) for pairwise comparison of models based on the validation scenario. Figure 19 presents the probability density functions of  $\log_{10}(\text{BF})$  over all perturbed velocity and pressure data sets in a three-by-three matrix. Here we compute four Bayes factors for each model against its counterpart. The significant levels in  $\log_{10}$ -scale, introduced by Jeffreys (1961) are marked with the vertical lines. Gray lines represent equally strong evidence for both models. Orange and red lines indicate thresholds for strong and decisive evidence in favor of one model against the other. Therefore, the Bayes Factor provides an objective measure of significance that quantifies the evidence in favor of one model’s superiority against another in the introduced uncertainty-aware Bayesian validation framework. The first plot in the second row, e.g., shows the distribution of  $\log_{10}(\text{BF})$  in favor of *Generalized IC* against *Classical IC*. This plot reveals that for all perturbed data sets, the Bayes factor is in the region where a strong evidence ( $\log_{10}(\text{BF})$  greater than two) exists in favor of *Generalized IC* to be better than *Classical IC*. Similarly, in all the analyzed cases (perturbed data sets), *pore-*



*network* model could be favored against *Classical IC* based on substantial evidence (the plot in the first column, the last row). Moreover, the distribution in the second row, third column of Figure 19 reveals that the Bayes factor distribution of *Generalized IC* against *pore-network* model proves a decisive evidence ( $\log_{10}(\text{BF})$  values greater than two) in favor of *Generalized IC*.



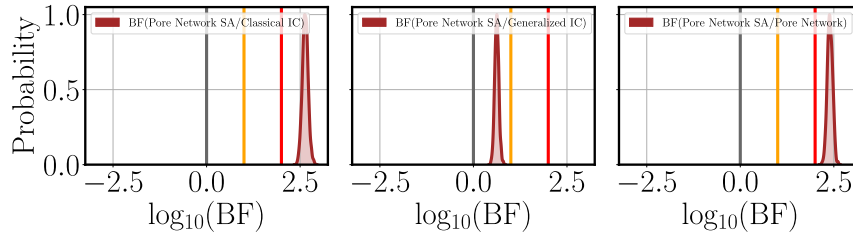
**Figure 19.** Distributions of  $\log_{10}$  (Bayes factor) for the pairwise comparison of competing models based on the validation scenario.

Table 6 presents a detailed statistical summary of the natural log of expected BME value and the expected model weights employed for model comparison analysis to obtain Figure 19. Additionally, use of the advanced surrogate representation provides a possibility to assess uncertainty of the BME values and the corresponding model weights. Therefore, Table 6 contains also information of such an post-calibration uncertainty with help of the deviation regarding 25% and 75% shown as sub- and superscripts, respectively. The expected model weights under noisy pore-scale data assumption convey a relatively clear model ranking in favor of *Generalized IC*, with *pore-network* model as second and *Classical IC* ranking last.

**Table 6.** The ranking based on the validation metrics.

Model	$\ln(\text{BME})$	Posterior weight
<i>Classical IC</i>	$100.930^{+0.09}_{-0.08}$	$0.327^{+0.0002}_{-0.0002}$
<i>Generalized IC</i>	$105.564^{+0.02}_{-0.02}$	$0.343^{+0.0002}_{-0.0001}$
<i>Pore-network</i>	$101.486^{+0.06}_{-0.07}$	$0.330^{+0.0001}_{-0.0002}$
<i>Pore-network SA</i>	$107.003^{+0.08}_{-0.08}$	-

The results presented so far are based on a comparison of the SRQs with averaged SRQs of the fully resolved Stokes simulation, as the Stokes–Darcy model with *Classical IC* and *Generalized IC* could offer a prediction on the REV scale only. However, the *pore-network* model could be directly compared to the reference data at the pore scale without volume averaging by calculating the surface-averaged pore-scale velocity at the pore-throat cross-sections. We will denote the *pore-network* model with pore-throat surface averaging model as *pore-network SA* model and the Bayes factors distribution is shown in Figure 20. This procedure emphasizes the advantage of the *Pore-network SA* over other discussed modeling concepts. The velocities of *Pore-network SA* model are not defined within the pore bodies but only at the pore throats, which explains why the results of Figure 20 show stronger evidence in favor of the *Pore network SA* model compared to other concepts. Table 6 also confirms our observation, where BME values rank the *Pore-network SA* model to the first place. Therefore, the original *Pore-network SA* model avoiding additional averaging step is a suitable approach when the detailed pore-scale information is available. Alternatively, Stokes–Darcy model with *Generalized IC* adequately represents the underlying physical processes once the REV scale information is available only.



**Figure 20.** Distributions of  $\log_{10}$  (Bayes factor) of the *pore-network* model without the surface averaging against competing models based on the validation scenario.

## 6 Summary and Conclusions

Models for coupling free flow with porous-medium flow contain various parametric uncertainties, particularly in the vicinity of the interface. We have offered a benchmark study that addresses these parametric uncertainties and conceptual modeling uncertainties reflecting different formulations of physical models. To do so, we have considered the Stokes–Darcy problem with different models for the porous-medium compartment and corresponding coupling strategies: the standard averaged model based on Darcy’s law with classical or generalized interface conditions as well as the pore-network model. To quantify the potential uncertainties of these three models, we have applied a Bayesian uncertainty-aware validation framework that assesses the performance of each model with respect to the reference data. The reference data for velocities and pressures have been obtained via a fully resolved pore-scale model. Since the task of calibration and validation in a probabilistic manner requires many model evaluations, we have employed a model reduction technique, namely Bayesian Sparse Polynomial Chaos Expansion, to accelerate the calculation.

Applying the suggested Bayesian validation framework, we have observed that the Stokes–Darcy model with the generalized interface conditions and the pore-network model can adequately capture the reference data during the calibration phase. However, the Stokes–Darcy model with the classical interface condition fails to approximate the reference velocity values in the deeper part of the porous medium during the calibration phase. Moreover, we have propagated the post-calibration parametric uncer-

tainty through each analyzed model to validate the different models against reference data that have not been used during the calibration phase. This uncertainty-aware Bayesian validation procedure has confirmed that the Stokes–Darcy model with the classical interface conditions has the most difficulties representing the underlying physical process correctly. Moreover, addressing the differences in the predictions of the considered modeling concepts, we have performed a Bayesian model comparison. This comparison reveals that the Stokes–Darcy model based on generalized interface conditions can represent processes on the REV scale best compared to the classical interface conditions or the correspondingly upscaled pore-network model. However, the pore-network model outperforms both Stokes–Darcy models with classical and generalized interface conditions once detailed pore-scale information is available. Concluding, we have observed that the suggested surrogate-based uncertainty-aware Bayesian validation framework helps to gain insights into underlying physical processes at acceptable computational costs.

## Acknowledgments

The work is funded by the Deutsche Forschungsgemeinschaft (DFG, German Research Foundation) – Project Number 327154368 – SFB 1313.

## References

- Angluin, D., & Smith, C. H. (1983). Inductive inference: theory and methods. *ACM Comput. Surv.*, 15(3), 237–269.
- Angot, P., Goyeau, B., & Ochoa-Tapia, J. A. (2017). Asymptotic modeling of transport phenomena at the interface between a fluid and a porous layer: jump conditions. *Phys. Rev. E*, 95, 063302.
- Angot, P., Goyeau, B., & Ochoa-Tapia, J. A. (2021). A nonlinear asymptotic model for the inertial flow at a fluid-porous interface. *Adv. Water Res.*, 149, 103798.
- Arjouni, Y., Kaabouch, N., El Ghazi, H., & Tamtaoui, A. (2017). Compressive sensing: performance comparison of sparse recovery algorithms. In *2017 IEEE 7th annual computing and communication workshop and conference (CCWC)* (pp. 1–7).
- Balhoff, M. T., Thomas, S. G., & Wheeler, M. F. (2007). Mortar coupling and up-scaling of pore-scale models. *Comput. Geosci.*, 12(1), 15–27.
- Balhoff, M. T., Thompson, K. E., & Hjortsø, M. (2007). Coupling pore-scale networks to continuum-scale models of porous media. *Computers & Geosciences*, 33(3), 393–410.
- Beavers, G. S., & Joseph, D. D. (1967). Boundary conditions at a naturally permeable wall. *J. Fluid Mech.*, 30, 197–207.
- Berger, J. O. (2013). *Statistical decision theory and Bayesian analysis*. Springer Science & Business Media.
- Beyhaghi, S., Xu, Z., & Pillai, K. M. (2016). Achieving the inside–outside coupling during network simulation of isothermal drying of a porous medium in a turbulent flow. *Transp. Porous Med.*, 114(3), 823–842.
- Blunt, M. J. (2017). *Multiphase flow in permeable media: a pore-scale perspective*. Cambridge University Press.
- Carraro, T., Goll, C., Marciniak-Czochra, A., & Mikelić, A. (2015). Effective interface conditions for the forced infiltration of a viscous fluid into a porous medium using homogenization. *Comput. Methods Appl. Mech. Engrg.*, 292, 195–220.
- Discacciati, M., & Gerardo-Giorda, L. (2018). Optimized Schwarz methods for the Stokes–Darcy coupling. *IMA J. Numer. Anal.*, 38, 1959–1983.
- Discacciati, M., Miglio, E., & Quarteroni, A. (2002). Mathematical and numerical models for coupling surface and groundwater flows. *Appl. Num. Math.*, 43, 57–

- Discacciati, M., & Quarteroni, A. (2009). Navier–Stokes/Darcy coupling: modeling, analysis, and numerical approximation. *Rev. Mat. Complut.*, 22, 315–426.
- Draper, D. (1995). Assessment and propagation of model uncertainty. *J. R. Stat. Soc. Ser. B. Stat. Methodol.*, 57(1), 45–70.
- Eggenweiler, E., & Rybak, I. (2020). Unsuitability of the Beavers–Joseph interface condition for filtration problems. *J. Fluid Mech.*, 892, A10.
- Eggenweiler, E., & Rybak, I. (2021). Effective coupling conditions for arbitrary flows in Stokes–Darcy systems. *Multiscale Model. Simul.*, 19(2), 731–757.
- Foreman-Mackey, D., Farr, W. M., Sinha, M., Archibald, A. M., Hogg, D. W., Sanders, J. S., . . . Pla, O. A. (2019). emcee v3: a Python ensemble sampling toolkit for affine-invariant MCMC. *Journal of Open Source Software*, 4(43), 1864.
- Gelman, A., Carlin, J. B., Stern, H. S., Dunson, D. B., Vehtari, A., & Rubin, D. B. (2013). *Bayesian data analysis*. CRC press.
- Geman, S., Bienenstock, E., & Doursat, R. (1992). Neural networks and the bias/variance dilemma. *Neural Comput.*, 4(1), 1–58.
- Goodman, J., & Weare, J. (2010). Ensemble samplers with affine invariance. *Commun. Appl. Math. Comput. Sci.*, 5(1), 65–80.
- Goyeau, B., Lhuillier, D., Gobin, D., & Velarde, M. (2003). Momentum transport at a fluid-porous interface. *Int. J. Heat Mass Transfer*, 46, 4071–4081.
- Hackbusch, W. (1989). On first and second order box schemes. *Computing*, 41(4), 277–296.
- Hanspal, N., Waghode, A., Nassehi, V., & Wakeman, R. (2009). Development of a predictive mathematical model for coupled Stokes/Darcy flows in cross-flow membrane filtration. *Chem. Eng. J.*, 149, 132–142.
- Harlow, F. H., & Welch, J. E. (1965). Numerical calculation of time-dependent viscous incompressible flow of fluid with free surface. *The Physics of Fluids*, 8(12), 2182–2189.
- Hills, R. G. (2006). Model validation: model parameter and measurement uncertainty. *J. Heat Transfer*, 128(4), 339–351.
- Hoeting, J. A., Madigan, D., Raftery, A. E., & Volinsky, C. T. (1999). Bayesian model averaging: a tutorial. *Statist. Sci.*, 14(4), 382–417.
- Hornung, U. (1997). *Homogenization and porous media*. Springer.
- Iooss, B., & Lemaître, P. (2015). A review on global sensitivity analysis methods. In G. Dellino & C. Meloni (Eds.), *Uncertainty management in simulation-optimization of complex systems: Algorithms and applications* (pp. 101–122). Springer US.
- Jäger, W., & Mikelić, A. (2000). On the interface boundary conditions by Beavers, Joseph and Saffman. *SIAM J. Appl. Math.*, 60, 1111–1127.
- Jäger, W., & Mikelić, A. (2009). Modeling effective interface laws for transport phenomena between an unconfined fluid and a porous medium using homogenization. *Transp. Porous Med.*, 78, 489–508.
- Jeffreys, H. (1961). *The theory of probability*. Oxford University Press.
- Kass, R. E., & Raftery, A. E. (1995). Bayes factors. *J. Amer. Statist. Assoc.*, 90(430), 773–795.
- Lācis, U., & Bagheri, S. (2017). A framework for computing effective boundary conditions at the interface between free fluid and a porous medium. *J. Fluid Mech.*, 812, 866–889.
- Lācis, U., Sudhakar, Y., Pasche, S., & Bagheri, S. (2020). Transfer of mass and momentum at rough and porous surfaces. *J. Fluid Mech.*, 884, A21.
- Le Bars, M., & Worster, M. (2006). Interfacial conditions between a pure fluid and a porous medium: implications for binary alloy solidification. *J. Fluid Mech.*, 550, 149–173.

- Liu, J. S. (2008). *Monte Carlo strategies in scientific computing*. Springer Science & Business Media.
- Lüthen, N., Marelli, S., & Sudret, B. (2021). Sparse polynomial chaos expansions: literature survey and benchmark. *SIAM/ASA J. Uncertainty Quantif.*, 9(2), 593–649.
- Mahadevan, S., & Rebba, R. (2005). Validation of reliability computational models using bayes networks. *Reliab. Eng. Syst. Saf.*, 87(2), 223–232.
- Marelli, S., & Sudret, B. (2015). *UQLab user manual–Polynomial chaos expansions* (Tech. Rep. No. UQLab-V0.9-104). ETH Zürich.
- Mehmani, Y., & Balhoff, M. T. (2014). Bridging from pore to continuum: a hybrid mortar domain decomposition framework for subsurface flow and transport. *Multiscale Model. Simul.*, 12(2), 667–693.
- Mehmani, Y., & Tchelepi, H. A. (2017). Minimum requirements for predictive pore-network modeling of solute transport in micromodels. *Adv. Water Resour.*, 108, 83–98.
- Mierzwiczak, M., Fraska, A., & Grabski, J. (2019). Determination of the slip constant in the Beavers–Joseph experiment for laminar fluid flow through porous media using a meshless method. *Math. Probl. Eng.*, 2019, 1494215.
- Mohammadi, F. (2020). *Development and realization of validation benchmarks*. (<https://arxiv.org/abs/2011.13216>)
- Oberkampf, W. L., & Barone, M. F. (2006). Measures of agreement between computation and experiment: validation metrics. *J. Comput. Phys.*, 217(1), 5–36.
- Oberkampf, W. L., & Roy, C. J. (2010). *Verification and validation in scientific computing*. Cambridge University Press.
- Oberkampf, W. L., & Trucano, T. G. (2008). Verification and validation benchmarks. *Nucl. Eng. Des.*, 238, 716–743.
- Ochoa-Tapia, A. J., & Whitaker, S. (1995). Momentum transfer at the boundary between a porous medium and a homogeneous fluid. I: theoretical development. *Int. J. Heat Mass Transfer*, 38, 2635–2646.
- Oladyshkin, S., De Barros, F., & Nowak, W. (2012). Global sensitivity analysis: a flexible and efficient framework with an example from stochastic hydrogeology. *Adv. Water Resour.*, 37, 10–22.
- Oladyshkin, S., Mohammadi, F., Kroeker, I., & Nowak, W. (2020). Bayesian3 active learning for the Gaussian process emulator using information theory. *Entropy*, 22(8), 890.
- Oladyshkin, S., & Nowak, W. (2012). Data-driven uncertainty quantification using the arbitrary polynomial chaos expansion. *Reliab. Eng. Syst. Saf.*, 106, 179–190.
- Oladyshkin, S., & Nowak, W. (2018). Incomplete statistical information limits the utility of high-order polynomial chaos expansions. *Reliab. Eng. Syst. Saf.*, 169, 137–148.
- Oladyshkin, S., & Nowak, W. (2019). The connection between Bayesian inference and information theory for model selection, information gain and experimental design. *Entropy*, 21(11), 1081.
- Oostrom, M., Mehmani, Y., Romero-Gomez, P., Tang, Y., Liu, H., Yoon, H., . . . Zhang, C. (2016). Pore-scale and continuum simulations of solute transport micromodel benchmark experiments. *Comput. Geosci.*, 20(4), 857–879.
- Patzek, T. W., & Silin, D. B. (2001). Shape factor and hydraulic conductance in noncircular capillaries: I. One-phase creeping flow. *J. Colloid Interface Sci.*, 236, 295–304.
- Robert, C., & Casella, G. (2013). *Monte Carlo statistical methods*. Springer Science & Business Media.
- Roy, C. J. (2019). Errors and uncertainties: their sources and treatment. In *Computer simulation validation* (pp. 119–141). Springer.
- Rybak, I., Schwarzmeier, C., Eggenweiler, E., & Rüde, U. (2021). Validation and

- calibration of coupled porous-medium and free-flow problems using pore-scale resolved models. *Comput. Geosci.*, 25(2), 621–635.
- Saffman, P. G. (1971). On the boundary condition at the surface of a porous medium. *Stud. Appl. Math.*, 50, 93–101.
- Scheibe, T. D., Murphy, E. M., Chen, X., Rice, A. K., Carroll, K. C., Palmer, B. J., ... Wood, B. D. (2015). An analysis platform for multiscale hydrogeologic modeling with emphasis on hybrid multiscale methods. *Groundwater*, 53(1), 38–56.
- Schöniger, A., Wöhling, T., & Nowak, W. (2015). A statistical concept to assess the uncertainty in Bayesian model weights and its impact on model ranking. *Water Resour. Res.*, 51(9), 7524–7546.
- Schöniger, A., Wöhling, T., Samaniego, L., & Nowak, W. (2014). Model selection on solid ground: rigorous comparison of nine ways to evaluate Bayesian model evidence. *Water Resour. Res.*, 50(12), 9484–9513.
- Smith, A. F., & Gelfand, A. E. (1992). Bayesian statistics without tears: a sampling–resampling perspective. *Am. Stat.*, 46(2), 84–88.
- Sobol’, I. (1993). Sensitivity estimates for nonlinear mathematical models. *Math. Model. Comput. Exp.*, 1(4), 407–414.
- Sudret, B. (2008). Global sensitivity analysis using polynomial chaos expansions. *Reliab. Eng. Syst. Saf.*, 93(7), 964–979.
- Terzis, A., Zarikos, I., Weishaupt, K., Yang, G., Chu, X., Helmig, R., & Weigand, B. (2019). Microscopic velocity field measurements inside a regular porous medium adjacent to a low Reynolds number channel flow. *Phys. Fluids*, 31, 042001.
- Tipping, M. E. (2001). Sparse Bayesian learning and the relevance vector machine. *J. Mach. Learn. Res.*, 1(3), 211–244.
- Tipping, M. E., Faul, A., Avenue, J. J. T., & Avenue, J. J. T. (2003). Fast marginal likelihood maximisation for sparse Bayesian models. In *Proceedings of the 9th international workshop on artificial intelligence and statistics* (pp. 3–6).
- Weishaupt, K., Joekar-Niasar, V., & Helmig, R. (2019). An efficient coupling of free flow and porous media flow using the pore-network modeling approach. *J. Comput. Phys. X*, 1, 100011, 21.
- Weishaupt, K., Terzis, A., Zarikos, I., Yang, G., Flemisch, B., de Winter, D. A. M., & Helmig, R. (2020). A hybrid-dimensional coupled pore-network/free-flow model including pore-scale slip and its application to a micromodel experiment. *Transp. Porous Media*, 135(1), 243–270.
- Wiener, N. (1938). The homogeneous chaos. *Am. J. Math.*, 60(4), 897–936.
- Xu, T., & Valocchi, A. J. (2015). A Bayesian approach to improved calibration and prediction of groundwater models with structural error. *Water Resour. Res.*, 51(11), 9290–9311.
- Yang, G., Coltman, E., Weishaupt, K., Terzis, A., Helmig, R., & Weigand, B. (2019). On the Beavers–Joseph interface condition for non-parallel coupled channel flow over a porous structure at high Reynolds numbers. *Transp. Porous Media*, 128, 431–457.
- Zampogna, G. A., & Bottaro, A. (2016). Fluid flow over and through a regular bundle of rigid fibres. *J. Fluid Mech.*, 792, 5–35.